NASA CR 72848
AMS 972

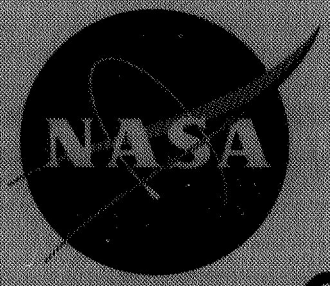

1970 Summary Of Combustion Instability Research At Princeton University

by

L. Crocco, D. T. Harrje, W. A. Sirignano,
F. V. Bracco, J. Lorenzetto,
S. N. Narayanan, T. J. Rosfjord, P. K. Tang,
T. S. Tonon, A. K. Varma

PRINCETON UNIVERSITY

prepared for

NATIONAL AERONAUTICS AND SPACE ADMINISTRATION

NASA Lewis Research Center
Grant NGL 31-001-155
Marcus Heidmann, Project Manager
Chemical Rockets Division

NOTICE

This report was prepared as an account of Government-sponsored work. Neither the United States, nor the National Aeronautics and Space Administration (NASA), nor any person acting on behalf of NASA:

A.) Makes any warranty or representation, expressed or implied, with respect to the accuracy, completeness, or usefulness of the information contained in this report, or that the use of any information, apparatus, method, or process disclosed in this report may not infringe privately-owned rights; or

B.) Assumes any liabilities with respect to the use of, or for damages resulting from the use of, any information, apparatus, method or process disclosed in this report.

As used above, "person acting on behalf of NASA" includes any employee or contractor of NASA, or employee of such contractor, to the extent that such employee or contractor of NASA or employee of such contractor prepares, disseminates, or provides access to any information pursuant to his employment or contract with NASA, or his employment with such contractor.

Requests for copies of this report should be referred to

National Aeronautics and Space Administration
Scientific and Technical Information Facility
P. O. Box 33
College Park, Md. 20740

NASA CR 72848
AMS 972

1970 SUMMARY OF COMBUSTION INSTABILITY RESEARCH AT PRINCETON UNIVERSITY

by

L. Crocco, D. T. Harrje, W. A. Sirignano,
F. V. Bracco, J. Lorenzetto, S. N., Narayanan,
T. J. Rosfjord, P. K. Tang, T. S. Tonon, A. K. Varma

PRINCETON UNIVERSITY
DEPARTMENT OF AEROSPACE AND MECHANICAL SCIENCES
Princeton, New Jersey 08540

prepared for

NATIONAL AERONAUTICS AND SPACE ADMINISTRATION

February 1971

GRANT NGL 31-001-155

NASA Lewis Research Center
Cleveland, Ohio
Marcus Heidmann, Project Manager
Chemical Rockets Division

TABLE OF CONTENTS

ABSTRACT

Five studies concerned with improving the understanding and control of combustion instability in liquid rocket engines are reported. The topics include: damping devices employing quarter-wave tubes and Helmholtz resonators, mass energy sources as investigated with a shock tube technique, unsteady diffusion flame studies relating to droplet and wave phenomena, the evaporization model as applied to the annular chamber, and a hydrogenation rocket feasibility study. Emphasis is placed on recent results and progress on each phase.

I. SUMMARY

Five research topics on the control and cause of combustion instability in liquid propellant rocket engines studied at Princeton University during 1970 under a continuing NASA Grant are extensively abstracted.

Theoretical and experimental studies governing quarter-wave tube and Helmholtz resonator efficiency are described and cross comparisons made. Although the peak of the real part of the acoustic admittance is higher for the quarter-wave tube and less volume is required for equivalent damping, a narrow frequency response limits application. Mass-energy sources at a number of engine locations have been determined via a step-shaped shock wave. The prior chamber conditions, the shock relations and the governing one-dimensional relations provide the means for this determination. Axisymmetric wake diffusion flame studies reveal significant interaction between the oscillation and the mixing and burning processes in the flow field. Velocity and temperature measurements are reported.

In an analytical study of nonlinear combustion instability, shock waves have been calculated by numerical methods for the annular chamber. The combustion model is based on droplet evaporation with more realistic assumptions. The feasibility of hydrogenation rocket principle was tested with negative results. Gas sampling was part of the test procedure.

II. INTRODUCTION

This report summarizes the research into the methods of controlling combustion instability,and into the underlying causes for the phenomena,performed at Princeton University during 1970 under a continuing NASA Grant. Five specific studies are reported. Each is presented in an extended abstract or condensed formal report format. When appropriate, the reader is referred to a more thorough reporting of the material presented herein. The purpose of this report is to present both the recent developments in instability research and a composite picture of the scope of the research conducted at Princeton.

A major portion of the research effort is in the area concerned with damping combustion driven oscillations. Helmholtz resonators, or liners when the resonators are used in great numbers, offer an attractive means of damping chamber pressure oscillations. Another means of damping pressure oscillations utilizes the quarter-wave tube. A variety of designs can be contemplated using the characteristics from both types of damping devices. The jet-flow model is used to describe the basic damping mechanism. Cross correlations help to point out the relative merits of each approach.

Considering the sources of energy necessary to "drive" the resonant combustion, several areas of active study are described.

After determining the steady-state combustion environment associated with like-impinging injector designs both theoretically and experimentally, a step-shock (shock wave followed by a uniform pressure) is being used diagnostically in the unsteady program. The strength of the shock is recorded as it approaches the near region of injection; also studied are the changes in the uniform pressure step. Marked changes in the shock amplitude are limited to the region close to the injector. The degree of energy addition governs whether the oscillation will continue. Steady-state data, the shock relations, the one-dimensional unsteady conservation equations and the instantaneous pressure records are used to determine the mass-energy sources.

Jet burning, such as with co-axial injector elements, and the burning in the wake of a propellant droplet form the basis for the jet diffusion flame experiment and the closely related analytical studies. A laminar fuel jet is burned in an oscillating oxidizer environment. At a well-defined frequency, combustion is enhanced and the flame shortens and broadens its profile. Special thermocouple and velocity probes, together with shadowgraph records, reveal the required detail to document the observations. The significant findings both analytically and experimentally offer one explanation for the instability coupling mechanism.

The nonlinear oscillations in an annular combustion chamber are examined by analytical means. The rate-controlling process is assumed to be the Priem-Heidmann type of droplet vaporization. A considerable effort was required to determine the proper perturbation approach. Numerical methods, together with this approach, reveal the anticipated shock-type waves for the annular motor configuration.

In the realm of different propulsion concepts hydrogenation of monopropellant decomposition was studied. The aim was to determine the feasibility of designing a high performance, low temperature engine with afterburning capability. Gas sampling, to reveal the composition of the combustion products, was central to the investigation.

III. QUARTER-WAVE TUBES VERSUS HELMHOLTZ RESONATORS: THEORIES, EXPERIMENTS, AND DESIGN CRITERIA

INTRODUCTION

In the development of acoustic liners for the suppression of rocket combustion instability, Helmholtz resonators have been the center of interest, both experimentally and theoretically. However, there are other types of damping devices which may be useful under certain conditions but have not yet been investigated to any great extent. A major portion of this work is devoted to the analytical study of the quarter-wave tube. Construction of the quarter-wave tube is quite simple. It is a slender tube with one end closed and the other end connected to the combustor; its length is one-quarter of the wavelength for which the device is designed to absorb and is shown in Fig. 1. The Helmholtz resonator is composed of a cavity and an orifice as also shown in the same figure.

Some general assumptions are made in the study of quarter-wave tube and Helmholtz resonators, both with short orifices[1] and with long orifices[2],[3]: 1) the flow inside the tube, or inside the orifice of the Helmholtz resonator, is one-dimensional, 2) heat transfer is neglected, frictional losses are not considered except in the analysis of the short orifice Helmholtz resonator[1], 3) the principal damping mechanism involves the loss of the jet kinetic energy when flow emerges from the tube into the chamber, or from the orifice into the chamber or cavity and hence is called the jet-flow model; nonlinear behavior of the flow is due to the jet formation and dissipation[4],[5], 4) the entropy is essentially unchanged; the production of entropy due to the kinetic energy loss of the jet is neglected since the gas volume in the chamber or in the cavity is much larger than the gas flow in the tube or in the orifice and finally 5) the gas is thermally and calorically perfect.

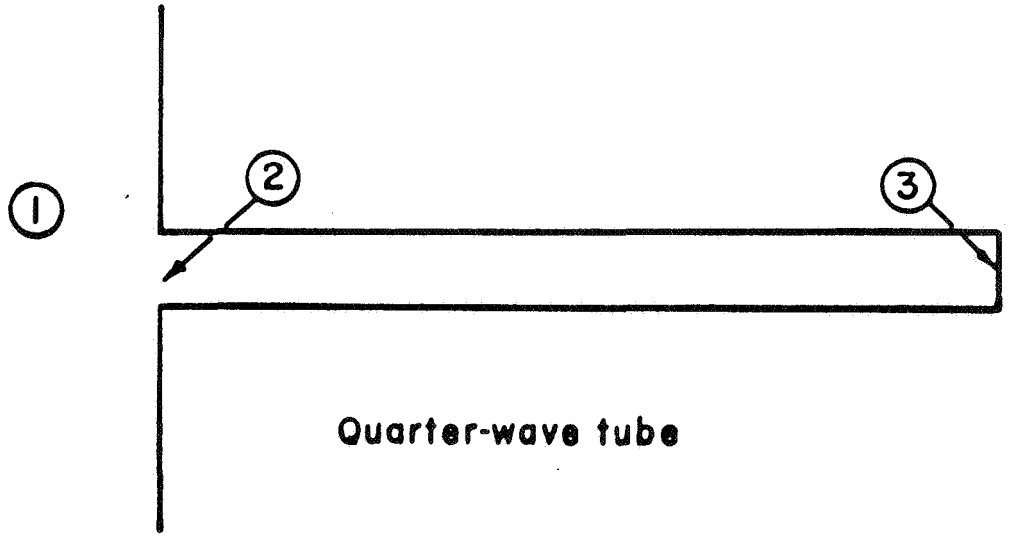

Quarter-wave tube

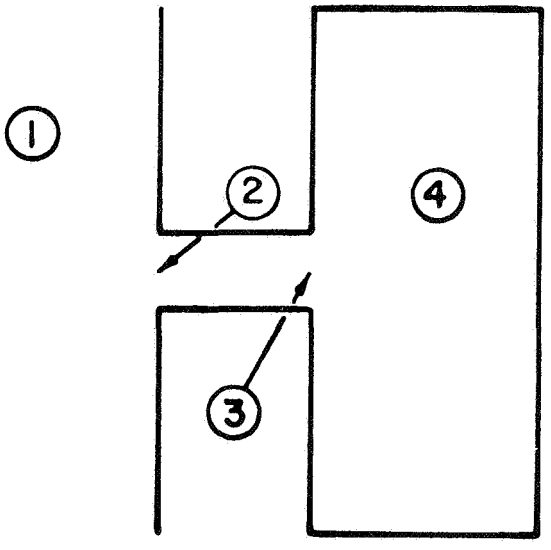

Helmholtz resonator

Figure 1

THEORY OF QUARTER-WAVE TUBE BEHAVIOR

The analytical works on Helmholtz resonators can be found in other publications[1],[2],[3] and will not be repeated here. For the quarter-wave tube, the governing equations are the one-dimensional continuity and frictionless momentum equations with the isentropic relation replacing the energy equation. After proper nondimensionalization and some manipulations, two first order wave equations are obtained for two unknowns, the speed of sound c and the gas velocity u, thus

$$\frac{f}{4}\frac{\partial}{\partial t}\left(c+\frac{\gamma-1}{2}u\right)+(c+u)\frac{\partial}{\partial x}\left(c+\frac{\gamma-1}{2}u\right)=0$$

$$\frac{f}{4}\frac{\partial}{\partial t}\left(c-\frac{\gamma-1}{2}u\right)-(c-u)\frac{\partial}{\partial x}\left(c-\frac{\gamma-1}{2}u\right)=0$$

where t and x are the dimensionless time and space coordinates and f is defined as the ratio of the frequency of the oscillation in the chamber to the quarter-wave tube resonant frequency which is in turn equal to the mean speed of sound divided by four times of the tube length. Proper boundary conditions are needed to solve these equations. At the end of the tube the gas velocity u_3 must be zero all the time. Subscript 3 denotes the closed end condition for a quarter-wave tube. At the chamber side of the tube, two different boundary conditions must be employed, depending on the flow direction. For flow entering the tube, the chamber and tube entrance conditions can be connected through the quasi-steady isentropic relation,

$$c_2^+ = p_1^{\frac{\gamma-1}{2\gamma}}\left[\frac{1-W_2^2}{1-W_1^2}\right]^{1/2}$$

where W is defined by the following relation

$$W^2=\frac{\gamma-1}{2}\left[u^2/p_1^{\frac{\gamma-1}{\gamma}}\right]\Big/\left[1+\frac{\gamma-1}{2}u_1^2/p_1^{\frac{\gamma-1}{\gamma}}\right]$$

and γ , p represent the specific heat ratio and pressure respectively. Superscript + indicates the relation is good only when flow is entering the tube. Subscripts 1 and 2 represent the conditions in the chamber and at the tube entrance. With flow coming out of the tube, the conditions at 1 and 2 are related by the following equation since the jet kinetic energy cannot be recovered:

$$c_2^- = \left[p_1 + \frac{1}{2} C_p \gamma p_1^{\frac{1}{\gamma}} u_1^2 \right]^{\frac{\gamma-1}{2\gamma}}$$

an average pressure coefficient C_p is introduced for we can visualize a certain cross-flow in the chamber over a "cylinder" formed by the jet column. Superscript - means the above equation is for outward flow.

The method of small perturbations is employed in solving this problem. Only the general approach and final results are discussed here. Further information can be found in other papers[6],[7]. The off-resonance solution is straightforward if the expansion parameter ϵ is the amplitude of the pressure oscillation in the chamber. This first order solution shows that the gas velocity at the tube entrance becomes infinite as the frequency approaches the resonant frequency and the phase between the pressure in the chamber and the gas velocity at the tube entrance is always 90 degrees out of phase. The jet dissipation and chamber flow (velocity) appear through the second-order boundary conditions so that second-order equations must be solved to see their effects. The result indicates that the real part of the acoustic admittance is relatively small except in the region close to resonance. The dotted curves in Figs. 2, 3, 4 and 5 are the off-resonance solutions for γ = 1.2 and ϵ = 0.1 and under various flow conditions. Up to this point we can conclude that the quarter-wave tube is a narrow-band device and thus this fact makes the near-resonance study more demanding.

We have already seen that the oscillation becomes infinite when the frequency of the oscillation in the chamber approaches the resonant frequency of the tube in the off-

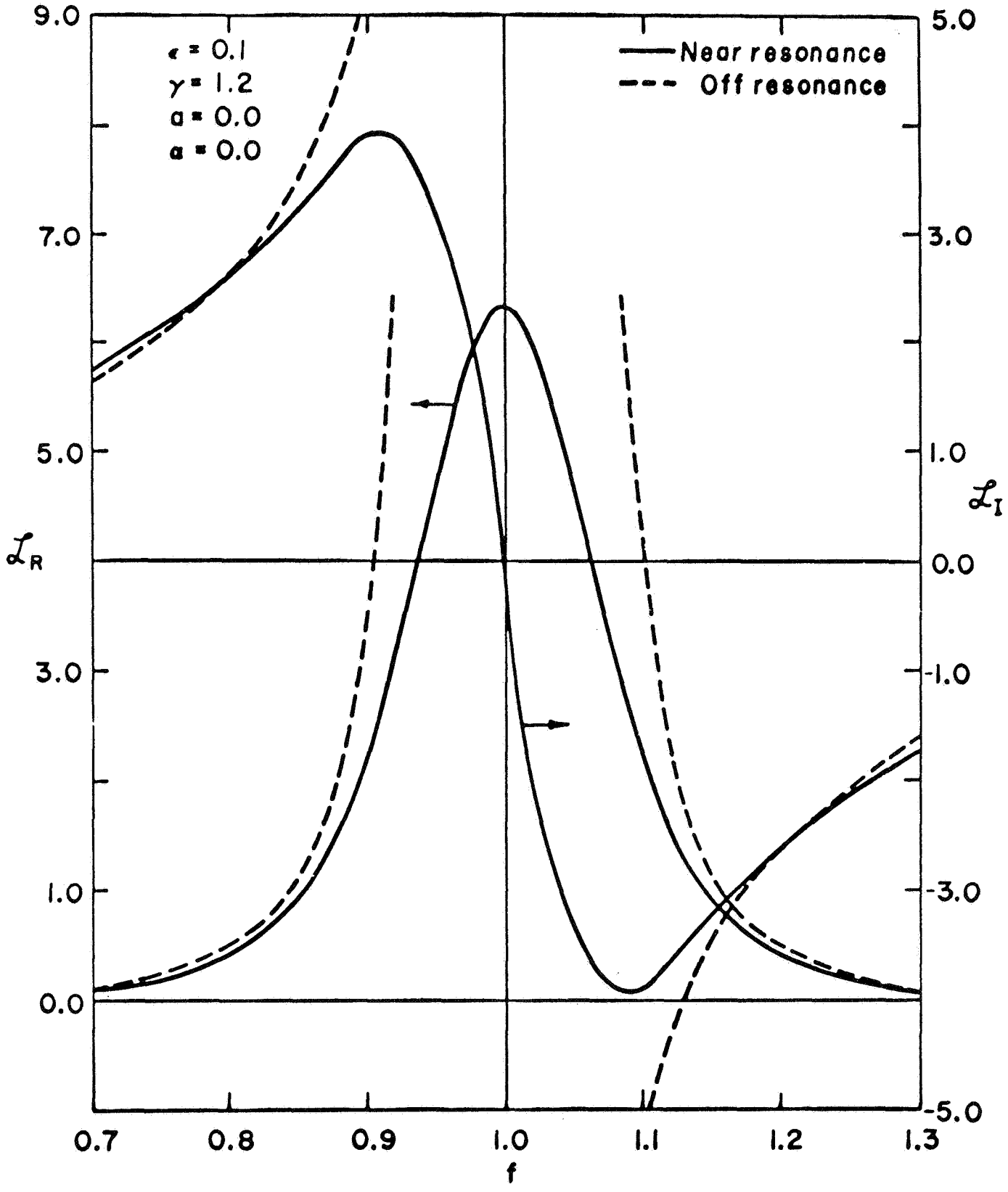
9.0
7.0
5.0
3.0
1.0
0.0
5.0
3.0
1.0
0.0
-1.0
-3.0
-5.0
$\mathcal{L}_R$
$\mathcal{L}_I$
$\epsilon = 0.1$
$\gamma = 1.2$
$a = 0.0$
$a = 0.0$
Near resonance
Off resonance
0.7
0.8
0.9
1.0
1.1
1.2
1.3
f

Figure 2

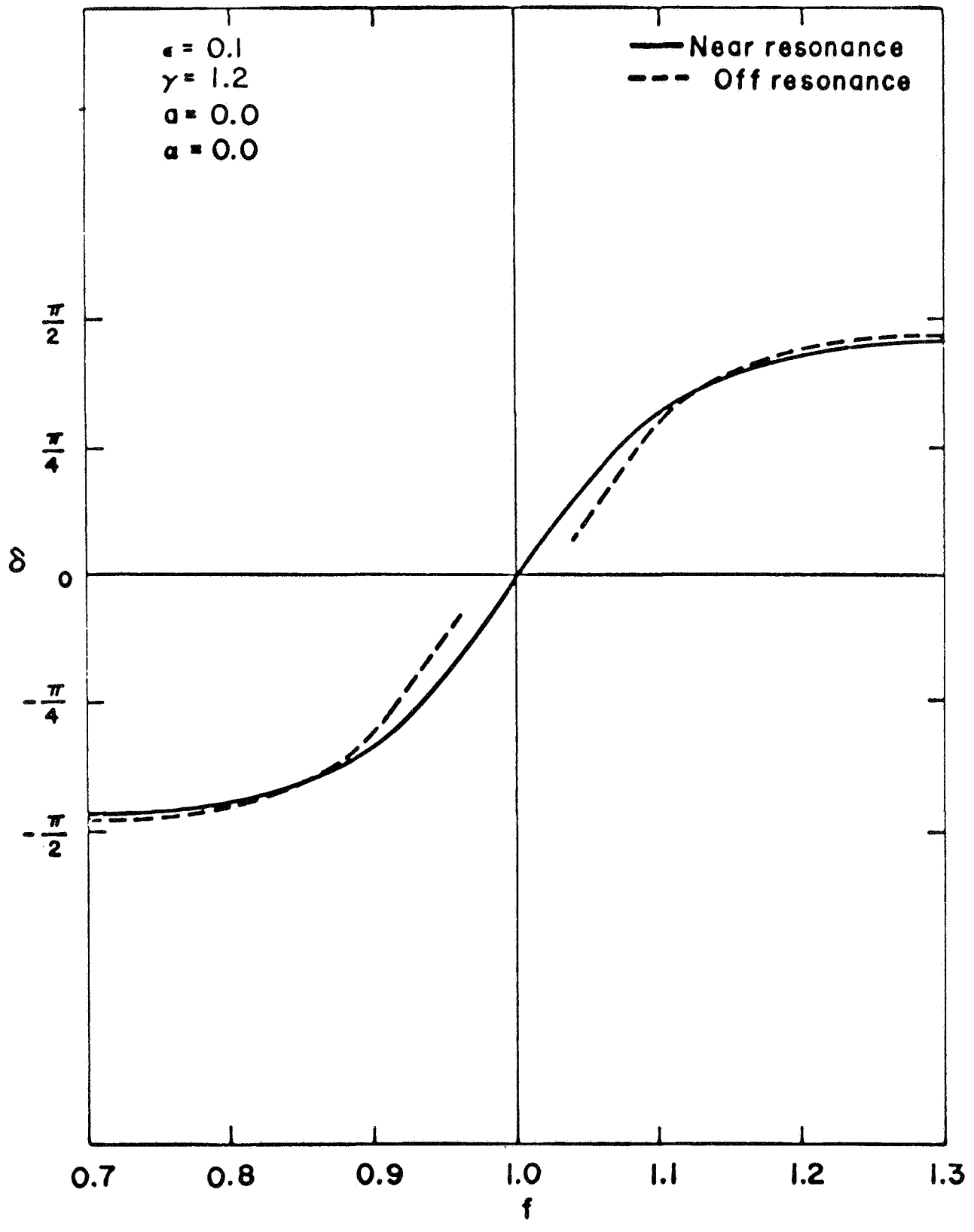

Figure 3

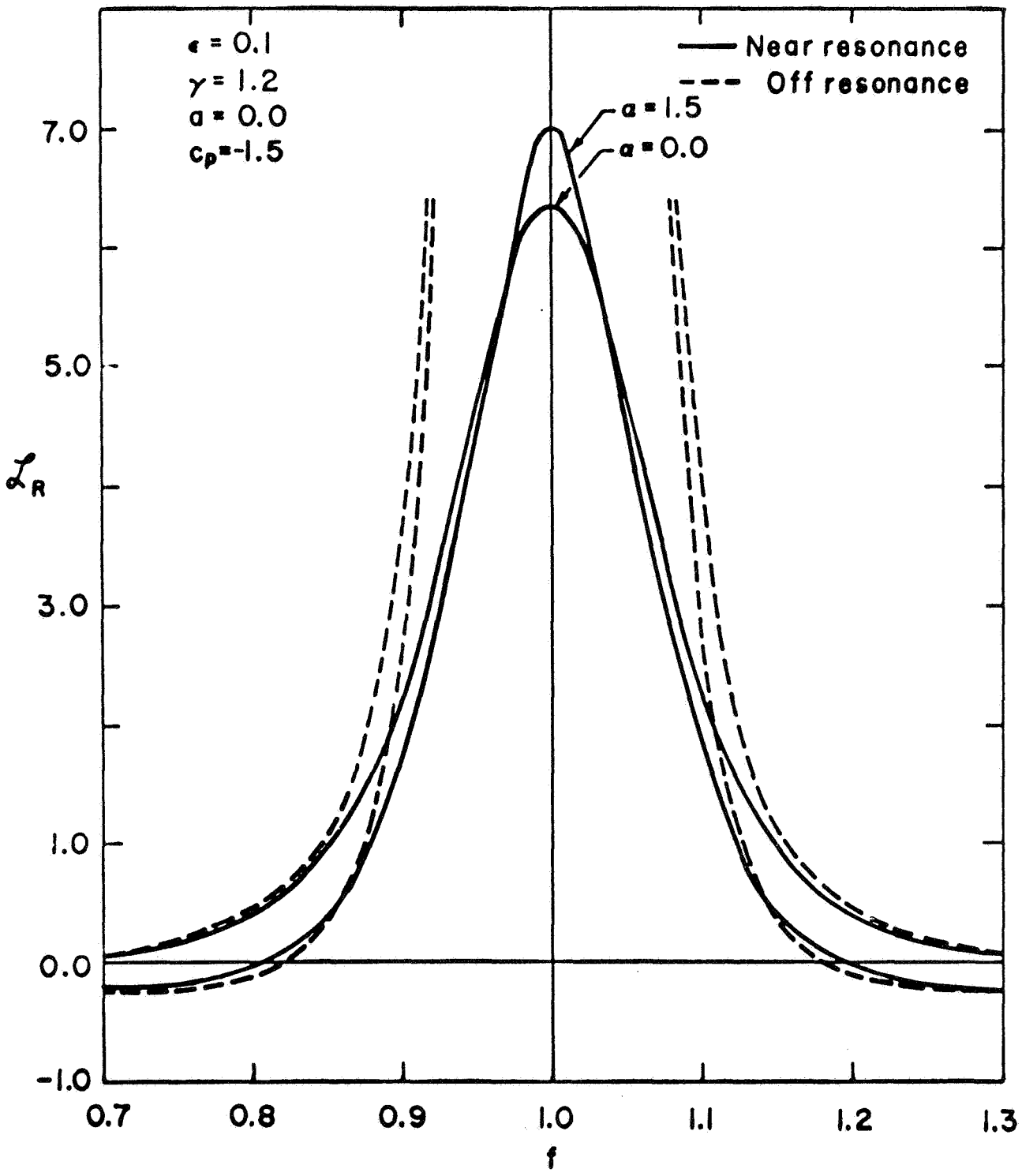
ε = 0.1
γ = 1.2
a = 0.0
c_p=-1.5
Near resonance
Off resonance
a = 1.5
a = 0.0
7.0
5.0
3.0
1.0
0.0
-1.0
$\mathcal{L}_R$
0.7
0.8
0.9
1.0
1.1
1.2
1.3
f

Figure 4

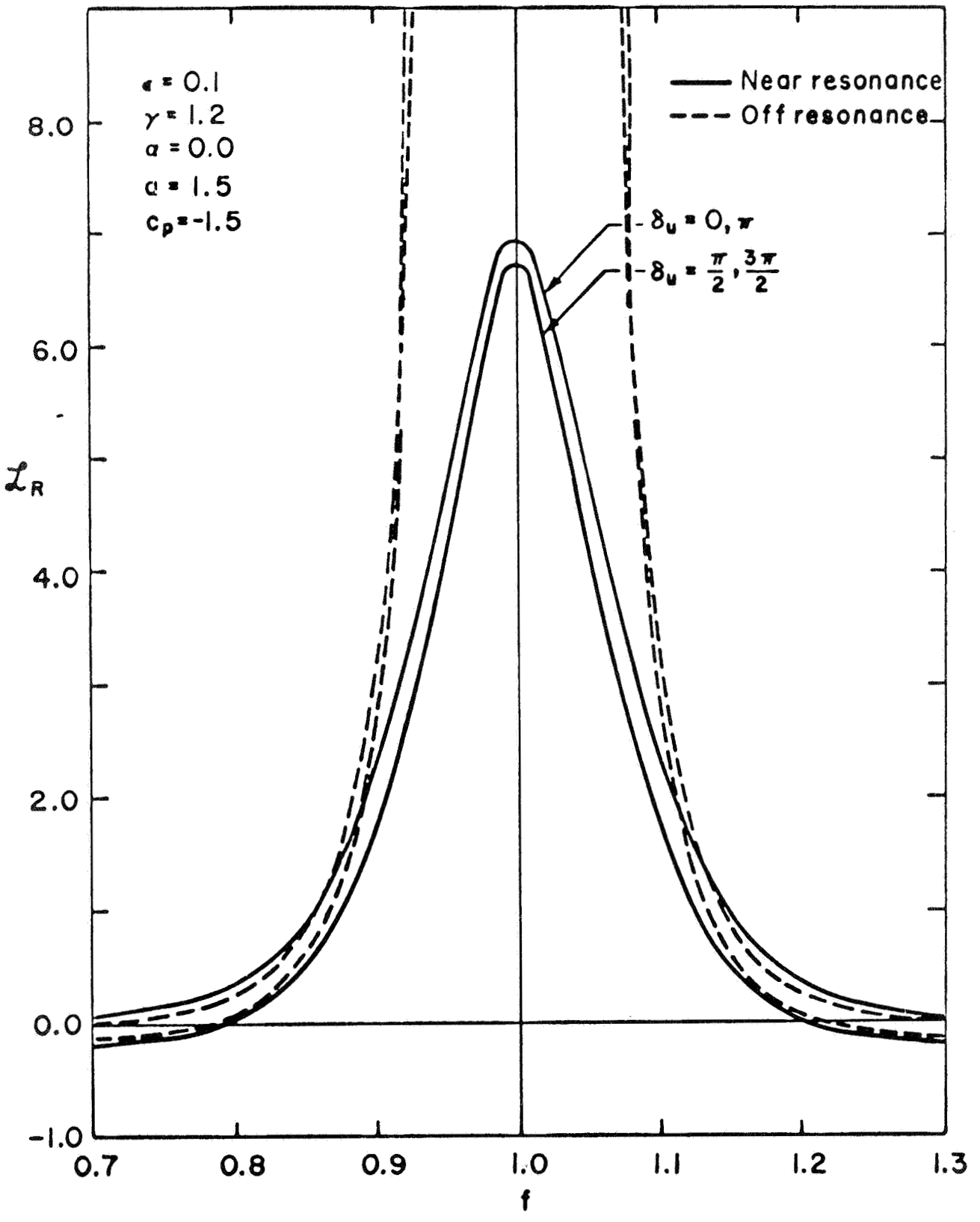

Figure 5

resonance study. From the physical point of view, however, this should not be the case since some dissipative effect would limit the growth of the oscillation. In this analysis the jet loss is assumed to be the only dissipative agent and therefore the oscillation will reach a maximum when the work done on the gas by the pressure oscillation is balanced by the jet dissipation.

It follows immediately that the expansion parameter should be the square root of the chamber pressure amplitude. It turns out that the first order unknown has to be determined by the second order analysis and an ordinary differential equation is obtained for that unknown, unlike the off-resonance study in which only algebraic equations are found. The first order solution shows that in addition to the fundamental, the first order wave has some higher odd harmonic components, even when the driving force (pressure oscillation in the chamber) is simply sinusoidal. This is not surprising because a quarter-wave tube also can resonate at any odd multiple of the fundamental frequency, i.e., 3/4, 5/4, 7/4, etc. The solid curves in Figs. 2, 3, 4, and 5 are the near-resonance solutions. The real and imaginary parts of the acoustic admittance, $\mathfrak{L}_R$ and $\mathfrak{L}_I$ are shown in Fig. 2 under no chamber flow condition. The curve of $\mathfrak{L}_R$ has a high peak but it decreases quite rapidly away from resonance. The phase δ between gas velocity at the tube entrance and the pressure oscillation in the chamber is given in Fig. 3. At resonance δ becomes zero and is about $\pm 90^\circ$ in off-resonance regions. With mean chamber flow, the peak of $\mathfrak{L}_R$ is even higher but the bandwidth is narrower with regard to frequency variation and negative $\mathfrak{L}_R$ is found in the off-resonance regimes, as shown in Fig. 4 where α represents the mean gas velocity and the Mach number of the mean chamber flow is product of ϵ and α. Fig. 5 shows the cases with velocity oscillation but without mean flow, a and δ_u denote the velocity amplitude and the phase between the gas

velocity and pressure oscillations in the chamber. For a travelling wave δ_u is either o or π and for a standing wave, it is either $\pi/2$ or $3\pi/2$. We can conclude that the effect of the gas velocity in the chamber induces a higher peak in α_R but at the same time gives negative α_R away from resonance. Similar phenomena are observed in the work on long-orifice Helmholtz resonators[2].

ACOUSTIC LINER EXPERIMENTS: QUARTER-WAVE TUBES AND HELMHOLTZ RESONATORS

Cold flow study with air at room temperature was performed on a tube with 0.325" ID, the frequency of oscillation was set on 400 Hz. The length of the tube could be varied by pushing a piston in and out of the tube and a pressure transducer was installed on the face of the piston. At resonance the tube length is about 8.48", change of f could be achieved by varying the tube length. The tube was located at the pressure anti-node of a resonant duct so that only the pressure oscillation was considered. The system was operated under the mean pressure of 40 psi. The description of the apparatus can be found in other works[8],[9] and is not given in detail here. Figs. 6a to 6e show the pressure amplitude at the tube end $\hat{p}_3$ versus the pressure amplitude in the duct $\hat{p}_1$, from both the theoretical calculation (curves) and experiment (dots) for different f. Starting from the exact resonance case f=1.0 (Fig. 6a), the experimental data follow the near-resonance solution quite well, and gradually the experiments turn away from the near-resonance solutions and come close to the off-resonance solutions, as seen in subsequent figures. We also notice that as the amplitude increases, the experimental data show a trend turning toward the near-resonance curves, this is in essence the broadening effect due to the increase in the resistance,which is found to be proportional to the gas velocity[5], a consequence of the jet-flow model.

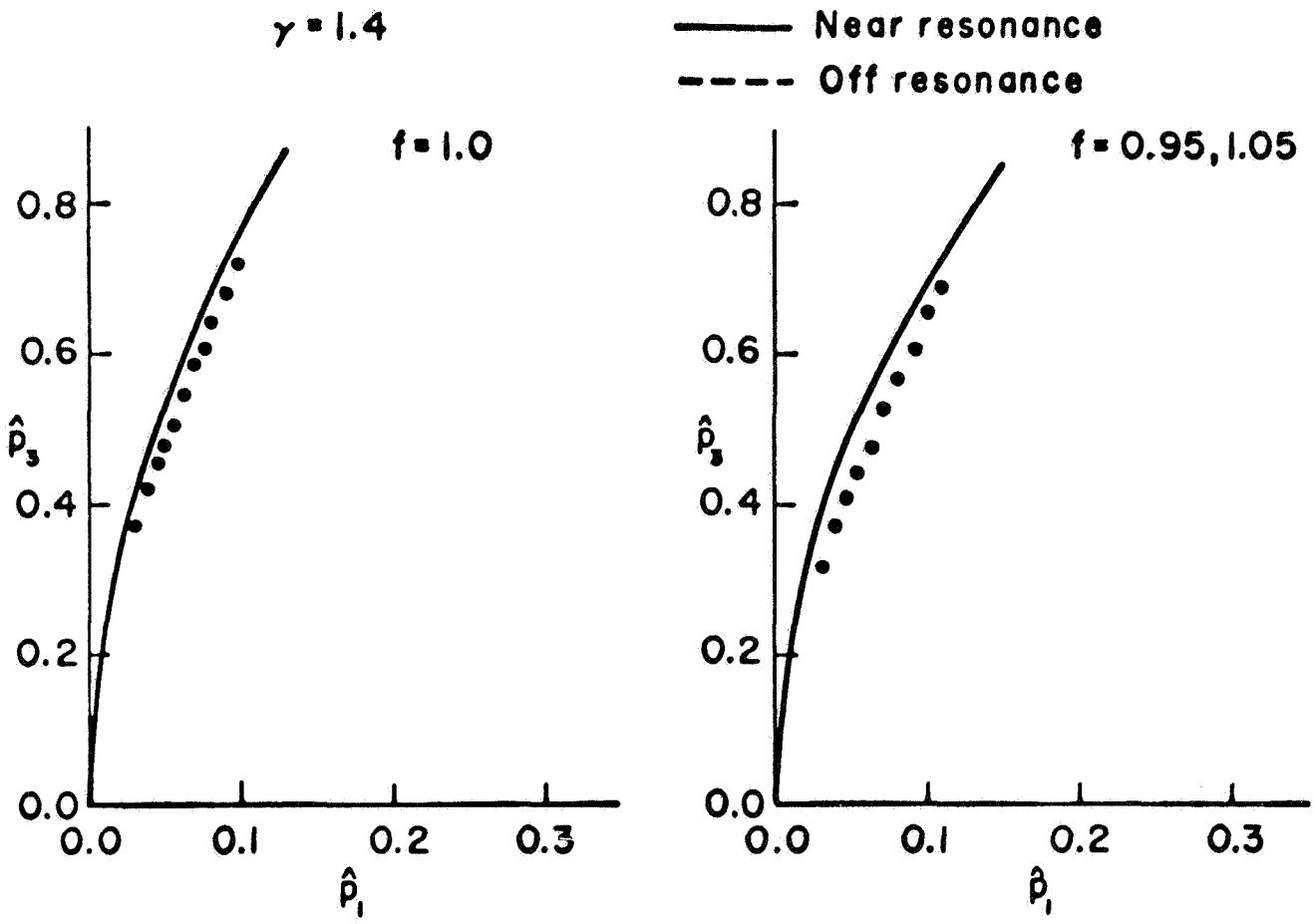

Figure 6a

Figure 6b

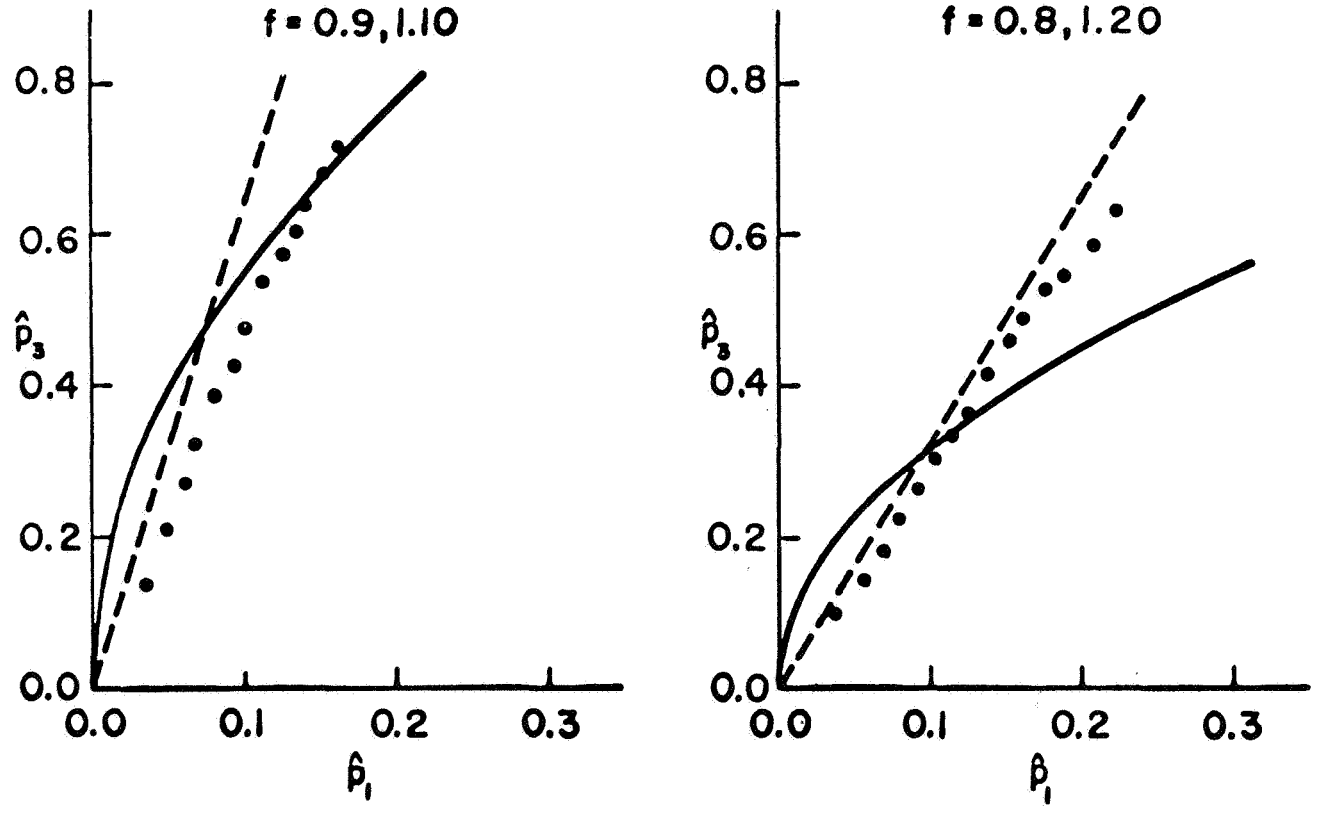

Figure 6c

Figure 6d

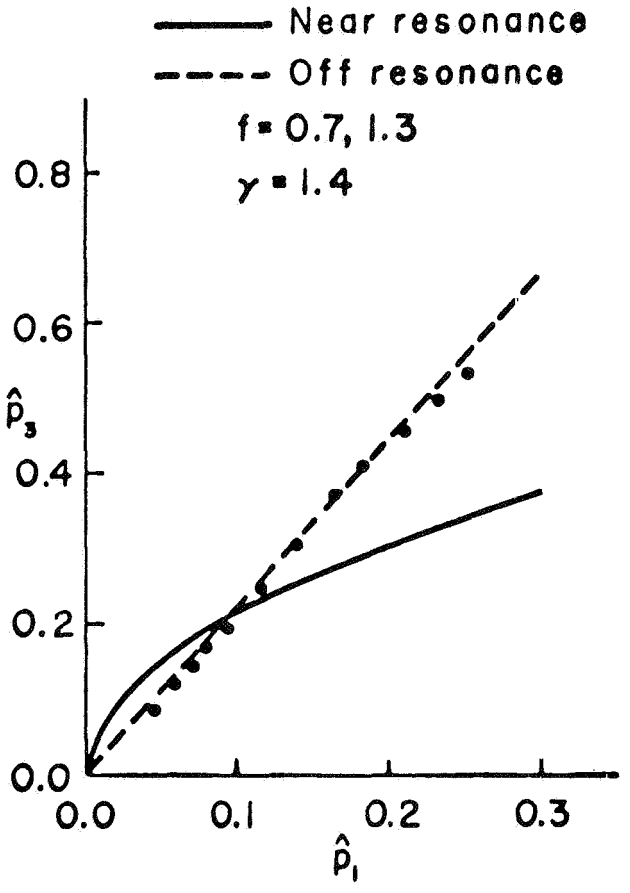
Near resonance
Off resonance
f = 0.7, 1.3
γ = 1.4
0.8
0.6
0.4
0.2
0.0
$\hat{p}_3$
0.0
0.1
0.2
0.3
$\hat{p}_1$

Figure 6e

A similar cold flow study for a Helmholtz resonator was conducted on the same apparatus. The orifice diameter d and cavity diameter D were fixed at 0.11" and 0.871" respectively but the orifice length ℓ could be changed by inserting blocks inside the cavity and variation of the cavity length L could be furnished by the in-and-out action of a piston inside the cavity. A pressure transducer was also installed on the piston face to pick up the cavity pressure variation. Tests were performed at two frequencies, 400 Hz and 770 Hz, the latter corresponds to the designed resonant frequency without end correction. The results of cavity pressure amplitude $\hat{p}_4$ versus duct pressure amplitude $\hat{p}_1$ are plotted in Figs. 7 to 10 in which an analytical calculation is based on the work for a short orifice[1] ($\ell \ll \lambda$) and with end correction (0.85d). For relatively large ℓ/d, the theory and experiment are in good agreement, as shown in Figs. 7a, 7b, 8a, 8b; on the other hand, the experimental points deviate significantly away from the analytical result as ℓ/d continuously decreases, as seen in Figs. 9a, 9b, 10a, 10b.

On the selection of the type of damping devices for practical purposes, we must consider at least two things: one is the performance, the other is the volume availability or weight limitation. Comparison of performance is given in Fig. 11 for a quarter-wave tube and a short orifice Helmholtz resonator. The real part of admittance was calculated for $\epsilon = 0.1$ and $\gamma = 1.4$. It is seen quite clearly that a Helmholtz resonator is a broad-band device with a smaller peak but a quarter-wave tube has a higher peak in $\mathcal{L}_R$ with a narrower bandwidth. To achieve maximum damping, we tend to use a device with high $\mathcal{L}_R$ such as a quarter-wave tube. But in practice, any slight uncertainty or deviation in frequency or gas temperature would result in a great loss of performance. The Helmholtz resonator is much less sensitive in this respect and should be considered in many situations. From the volume consideration, we see that by minimizing the volume of a long orifice Helmholtz resonator, it turns out that the minimum is

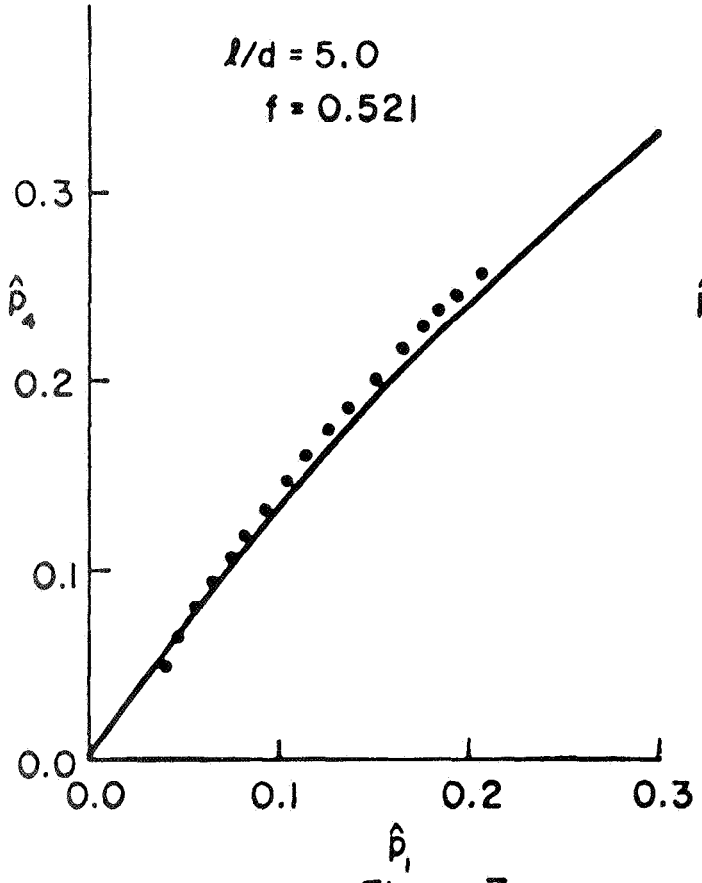

Figure 7a

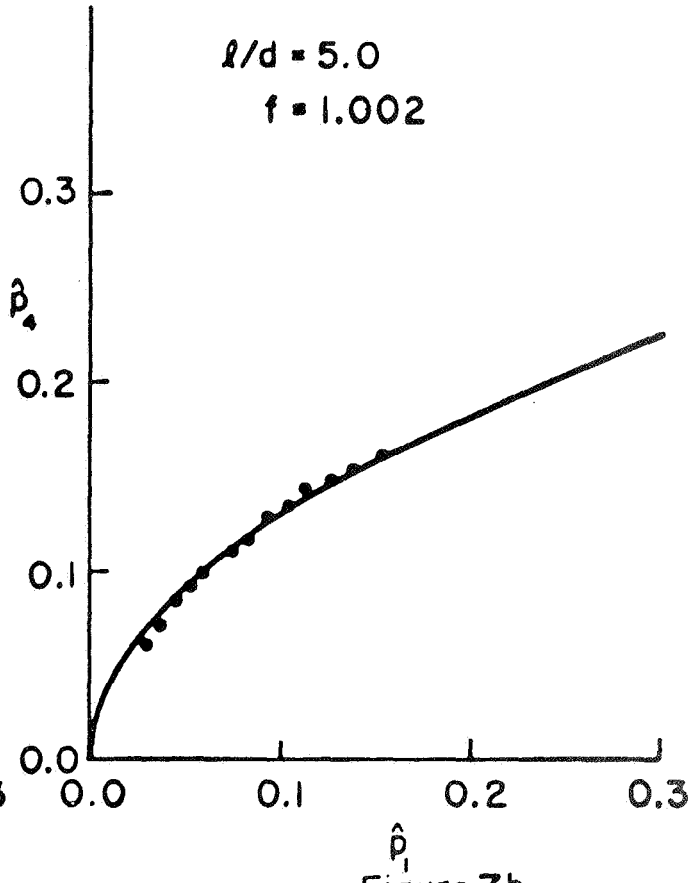

Figure 7b

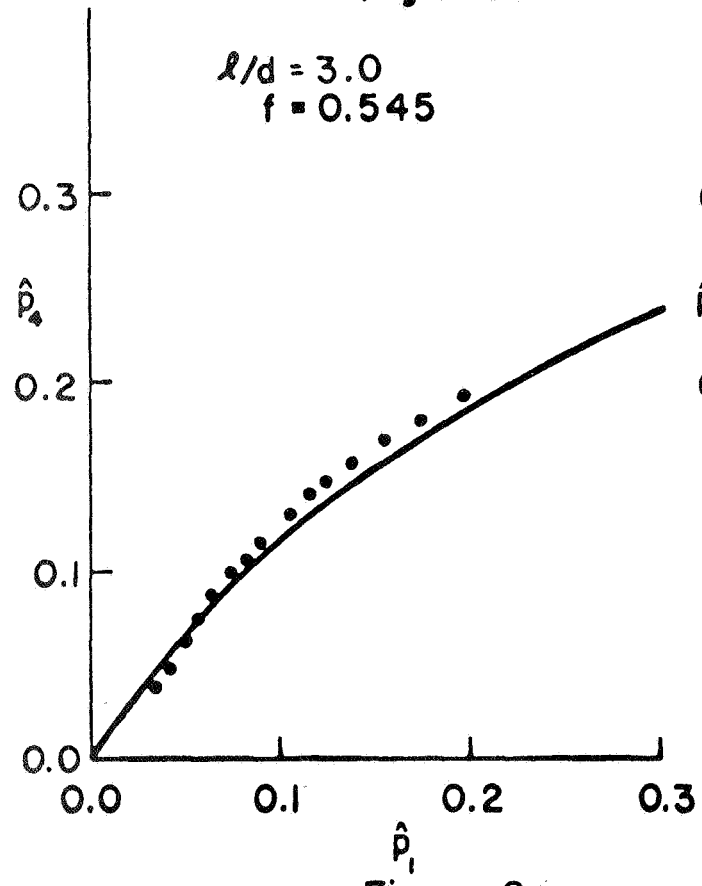

Figure 8a

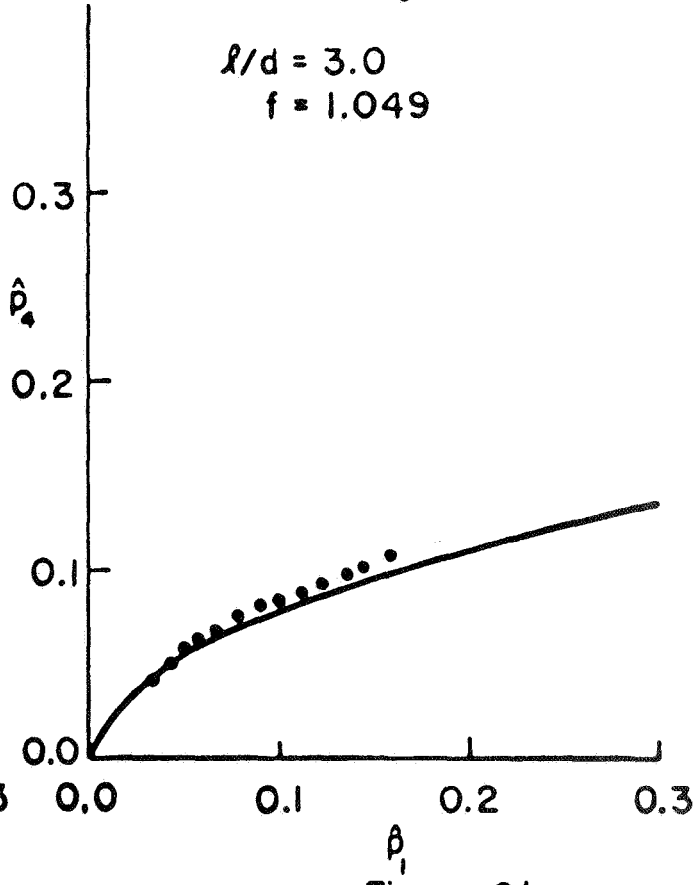

Figure 8b

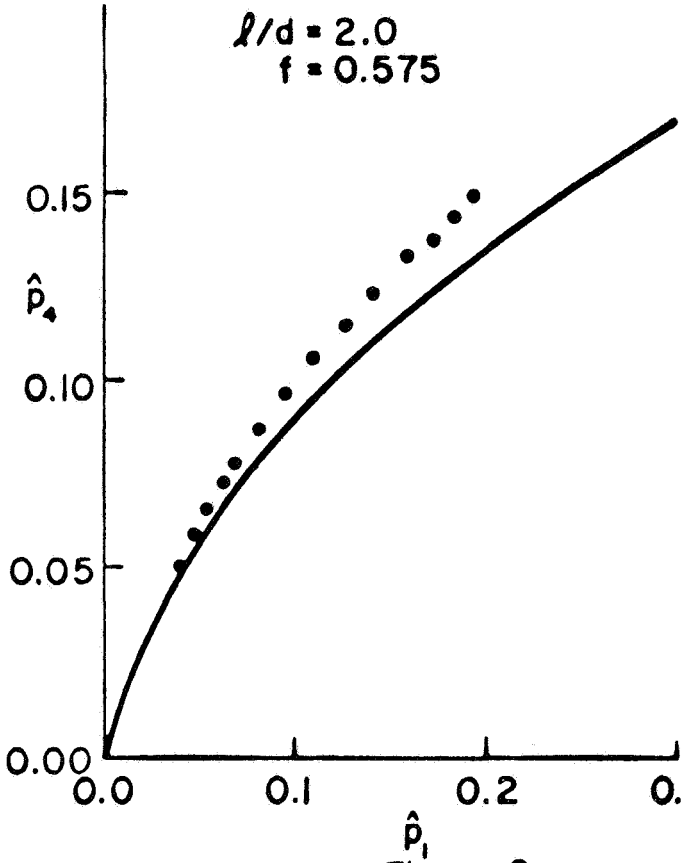

Figure 9a

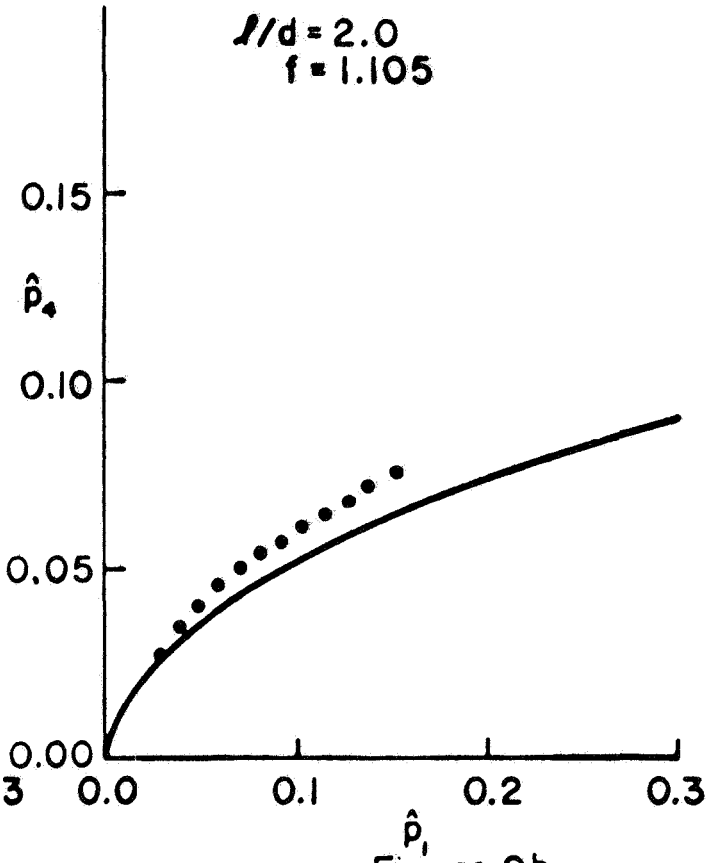

Figure 9b

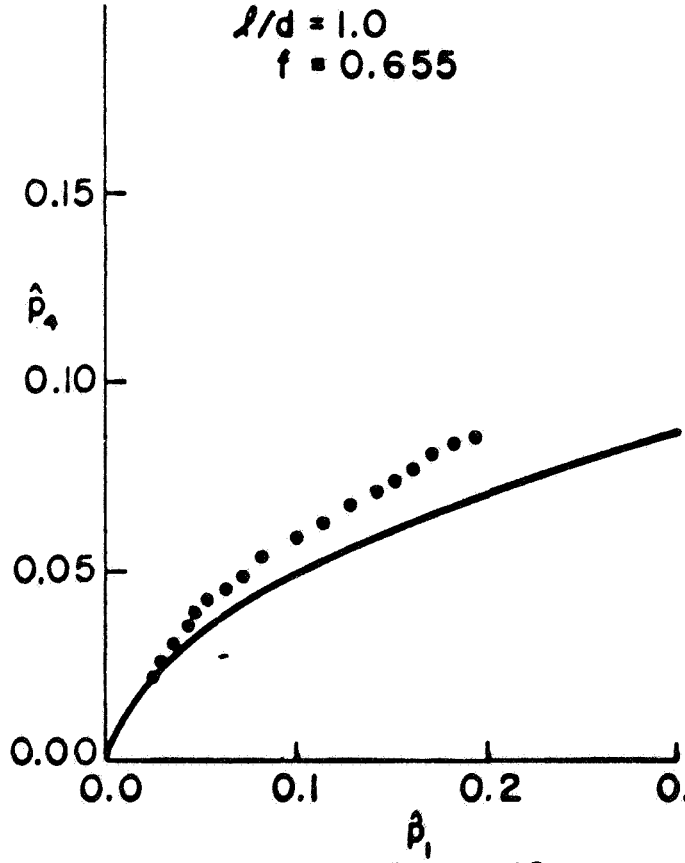

Figure 10a

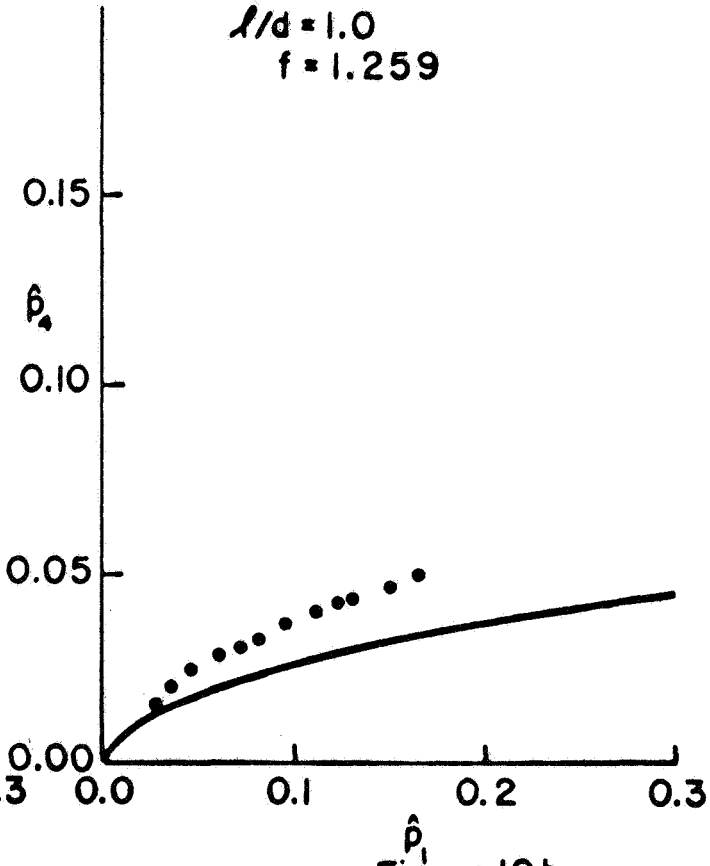

Figure 10b

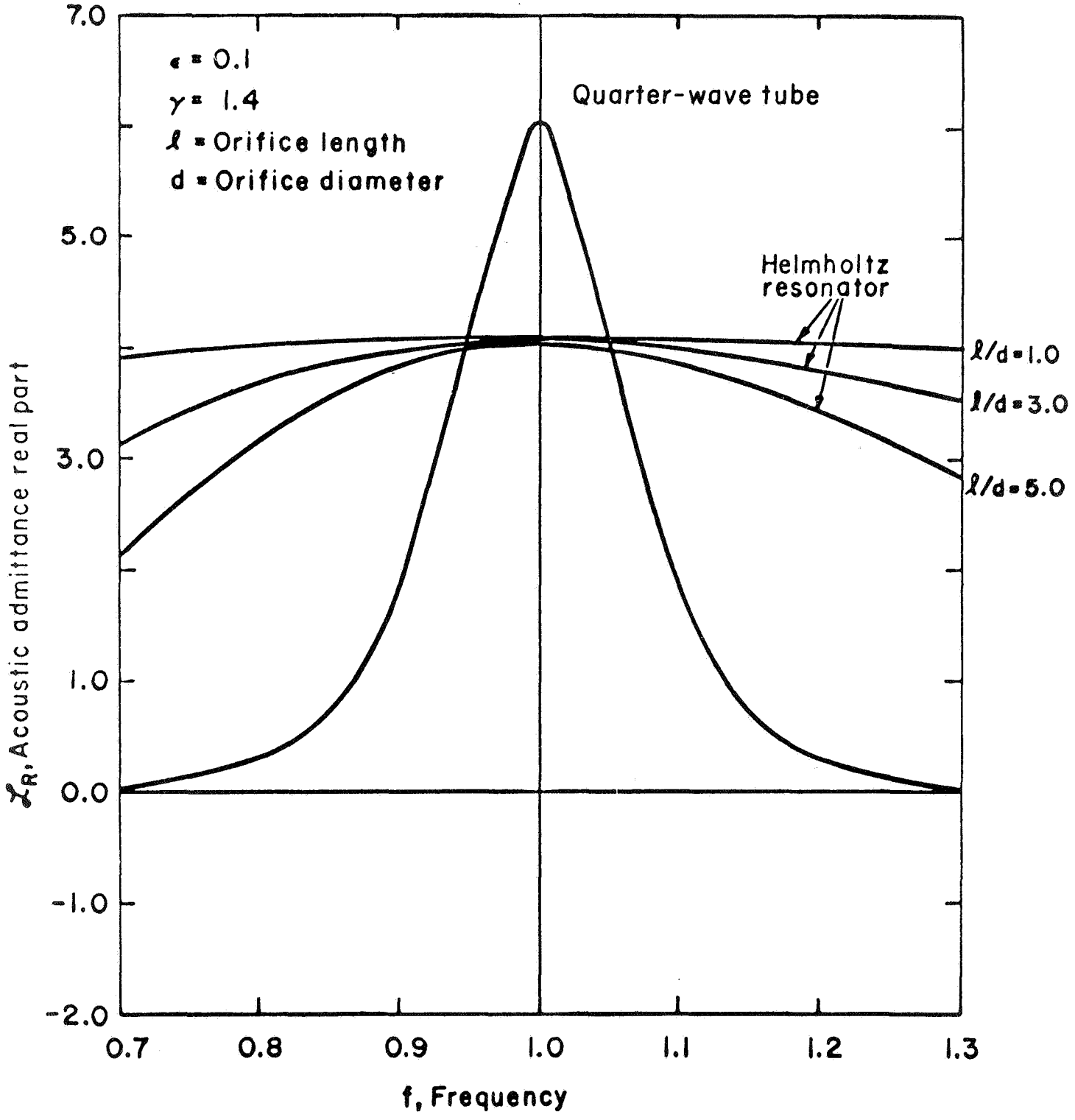
7.0
5.0
3.0
1.0
0.0
-1.0
-2.0
0.7
0.8
0.9
1.0
1.1
1.2
1.3
ε = 0.1
γ = 1.4
ℓ = Orifice length
d = Orifice diameter
Quarter-wave tube
Helmholtz resonator
ℓ/d = 1.0
ℓ/d = 3.0
ℓ/d = 5.0
$\mathcal{L}_R$, Acoustic admittance real part
f, Frequency

Figure 11

equal to the volume of the quarter-wave tube. Another factor we must consider is the accessibility of the damping device to a given area. Because of the inherent opening area ratio with the Helmholtz resonator, we can put more quarter-wave tubes on a finite surface than Helmholtz resonators. To improve the frequency response with quarter-wave tubes, this can be accomplished if an array of tubes tuned at different frequencies are used. In conclusion, we can have certain flexibilities at our disposal to apply various damping devices in any particular problem.

DESIGN PROCEDURES

From the theoretical developments described in References 1-3 and elsewhere, certain design procedures can be extracted. Reference 10 contains such an extraction and presents several comprehensive design procedures. In addition to volume and response considerations mentioned earlier, the designer should have some idea as to the sufficient amount of liner damping required to render a given rocket motor stable. All three aspects of the design problem are considered in Reference 10.

The designer is usually interested in a design that is optimum in some sense. There are usually certain constraints imposed upon a given problem, and the particular constraints vary from problem to problem. An optimal design procedure that considers a wide class of possible constraints is now presented. The following procedure is optimal in the sense that the required lined surface area is minimized. The design variables are considered to be A the orifice cross-sectional area, ℓ the orifice length, V the cavity volume (for 1/4-wave tubes, $V = o$ and $\ell = \lambda/4$), f_L the fraction of chamber wall area that is lined, σ the percent open area ratio of the liner, and the position of the liner in the chamber. The design procedure consists of satisfying the following three conditions simultaneously:

1) choose any value of A, ℓ, V such that $A\lambda/V = 2\tan(2\pi\ell/\lambda)$

2) choose any value of ℓ, f_L, σ such that

$$f_L\sigma > \frac{\epsilon_o \bar{c}_{1\ell} G}{\gamma_{1a}\bar{c}_{1a}C_1C_2M}\left[1 - \left(\frac{\nu}{S_{\nu\ell}}\right)^2\right]$$

3) place any lined surface in areas at or very near the region where the unstable pressure oscillations are largest.

Only circular-cylindrical combustors are considered here, although other geometries are treated in Reference 10. In the above expressions, λ is the wavelength of oscillation, ϵ_o the maximum value of the square root of the nondimensional pressure amplitude expected or allowed in the chamber, $\bar{c}_{1\ell}$ the chamber speed of sound local to the lined surface, $\bar{c}_{1a}$ the average chamber speed of sound, γ_{1a} the average value of the ratio of specific heats in the chamber, C_1 and C_2 design factors that account for differences in mean temperature, molecular weight, and ratio of specific heats between fluid in the backing volume and fluid in the local chamber environment. If the mean temperature and molecular weight in the backing volume are the same as those in the local chamber environment, $C_1 = 1.0$, otherwise $C_1 = 0.65$. If the ratio of specific heats in the backing volume is the same as that in the local chamber environment, or if $\ell/\lambda < 0.1$, $C_2 = 1.0$, otherwise $C_2 = 0.2$. The integer ν describes the tangential character of the mode, $S_{\nu\ell}$ the eigenvalue of the mode, and M and G are defined below.

$$M = \left\{3C_D^2\pi/\left[2\gamma_{1\ell}\left(1 + |\cos^3(2\pi\ell/\lambda)|\right)\right]\right\}^{1/2}$$

$$G = -(\gamma_{1a}+1)\bar{M}_e/2X + \mathcal{E}_R/2X + \gamma_{1a}\bar{M}_e n(1-\cos\omega\tau)/2X$$

In these last expressions, C_D is the coefficient of discharge for the orifice to be used when $\ell/\lambda < 0.1$, otherwise $C_D = 1$. $\bar{M}_e$ is the mean chamber Mach number at the nozzle entrance, $\mathcal{E}_R$ is the real part of the nozzle admittance, X is the chamber length (or combustion length if shorter than the chamber length), ω the radian frequency of instability,

and n and τ are the interaction index and sensitive time lag of the Crocco $n-\tau$ theory. In the above expression for G, only transverse modes are considered and the effect of droplet drag has been omitted. Such restrictions are not present in Reference 10.

Condition (1) requires that the liner geometry be the resonant geometry. Condition (2) provides a criteria for the minimum amount of lined surface area required. Condition (3) insures that the liner will be used in a most efficient manner. The reasoning that leads to the above three conditions can be found in Reference 10 .

The quantity M is directly proportional to the real part of the admittance and (as mentioned previously) becomes largest when $\ell/\lambda = 1/4$. Condition (2) then says that the product $f_L \sigma$ is minimized (for variation of only ℓ/λ). Thus, the fact that the quarter-wave tube provides for minimum surface area in addition to minimum volume should urge the designer to seriously consider such devices in design.

Condition (1) makes no distinction between the various geometrical forms the liner may assume (Helmholtz resonators, 1/4-wave tubes, etc.). In the underlying theory, the dimensions of the cavity volume (for Helmholtz resonators) must be small compared to the wavelength. However, in the quasi-steady limit $\ell/\lambda \to 0$, Condition (1) requires that V become very large, in such case the previously stated restriction cannot be satisfied. It is found that Condition (1) (and the expression for M) gives accurate results for orifice-mean-flow velocities less than about one-third of the oscillatory velocity. Because of Condition (3), the effects of chamber flow do not alter Conditions (1) and (2). Large orifice-mean-through flows, and chamber flows are considered in Reference 10 where important. Oversizing of holes in cavity-volume-limited situations, evaluation of a given liner design, and other practical problems are also considered in Reference 10.

IV. UNSTEADY MASS-ENERGY SOURCE DETERMINED BY A SHOCK TUBE TECHNIQUE

INTRODUCTION

A LOX/ethanol motor with radial nozzles and a shock tube mounted at the nozzle end was used to determine the unsteady mass-energy source. The chamber pressure was 60 psia, the nozzle entrance Mach number was .314 and the mixture ratio was 1.6. The injector consisted of a 4x4 matrix of like-on-like impinging doublets. Helium was used as the driving gas. At the breaking of the diaphragm, a step shock is generated at the nozzle end of the motor. The pressure ratio through the shock front far from the injector, is 1.5. As the step shock moves toward the injector, its amplitude and its shape are modified due to its interaction with the combustion process. The amplitude of the shock front is practically unchanged up to a few inches from the injector where it rapidly starts increasing to double just before reflecting against the injector face. The pressure after the front undergoes more complicated changes. The shock pressure versus time was thus measured at several distances from the injector. The function $p=p(x,t)$ and the shock velocity were thus experimentally determined. Knowing $p=p(x,t)$ and the steady state ahead of the shock, the following dimensionless unsteady equations were numerically solved for $\rho=\rho(x,t)$, $u=u(x,t)$, and $Q=Q(x,t)$;

$$\rho_t + (\rho u)_x = Q$$

$$\rho(u_t + u u_x) + \frac{p_x}{\gamma} = 0$$

$$\frac{p_t}{\gamma} + \frac{u p_x}{\gamma} + p u_x = Q$$

Q is the dimensionless unsteady mass-energy source, p is the gas pressure, ρ is the gas density, u is the gas velocity, and t is time. The quantity $(\ )_t$ stands for $\partial(\ )/\partial t$. The main purpose of this experiment is that of studying the relation between the unsteady mass-energy source and the unsteady gas environment.

EXPERIMENTAL PROGRAM

The experimental hardware used in the test program is shown in Fig. 12. The shock tube extends from the test cell. This tube is operated at high pressure and filled with helium to maintain a speed of sound close to that found in the hot chamber. The burst disc which separates the shock tube from the rocket chamber burns through after approximately 200 milliseconds of test operation, thus generating the step shock. The rocket chamber, in which the precise pressure measurements are made, constitutes the left portion of the figure. Combustion gases exhaust from the centrally-positioned radial nozzle.

The physical interpretation of the recorded shock is obtained through the use of Fig. 13. Steady-state studies show that most of the steady combustion has been completed in region a . Region b is necessary for the complete formation of the step shock. As the disc breaks, part of the helium rushes out of the nozzle and part of it rushes toward the injector. The combustion gases are thus prevented from reaching the nozzle and a shock is progressively formed in Region b. Fig. 13 shows a characteristic shock history in that as an expansion wave moves into He, a shock wave moves into the combustion gases, a contact discontinuity is present (between He, and combustion products). The interesting events occur when the shock enters Region a (region of active combustion). As the shock enters the non-uniform region, where liquid fuel is present, acoustic waves are generated due to the non-uniformity of the gas ahead of the shock and further combustion of the fuel (R). Notice that a transducer positioned at x_t would see no shock for $t_1 \leq t < t_2$, and then would see a shock arriving at $t = t_2$. Next a flat step shock would be recorded for $t_2 \leq t < t_3$. Finally, at $t = t_3$, the transducer would start recording the effect of combustion until $t = t_4$, when the reflected shock arrives. Notice that even though a transducer is out of the combustion zone

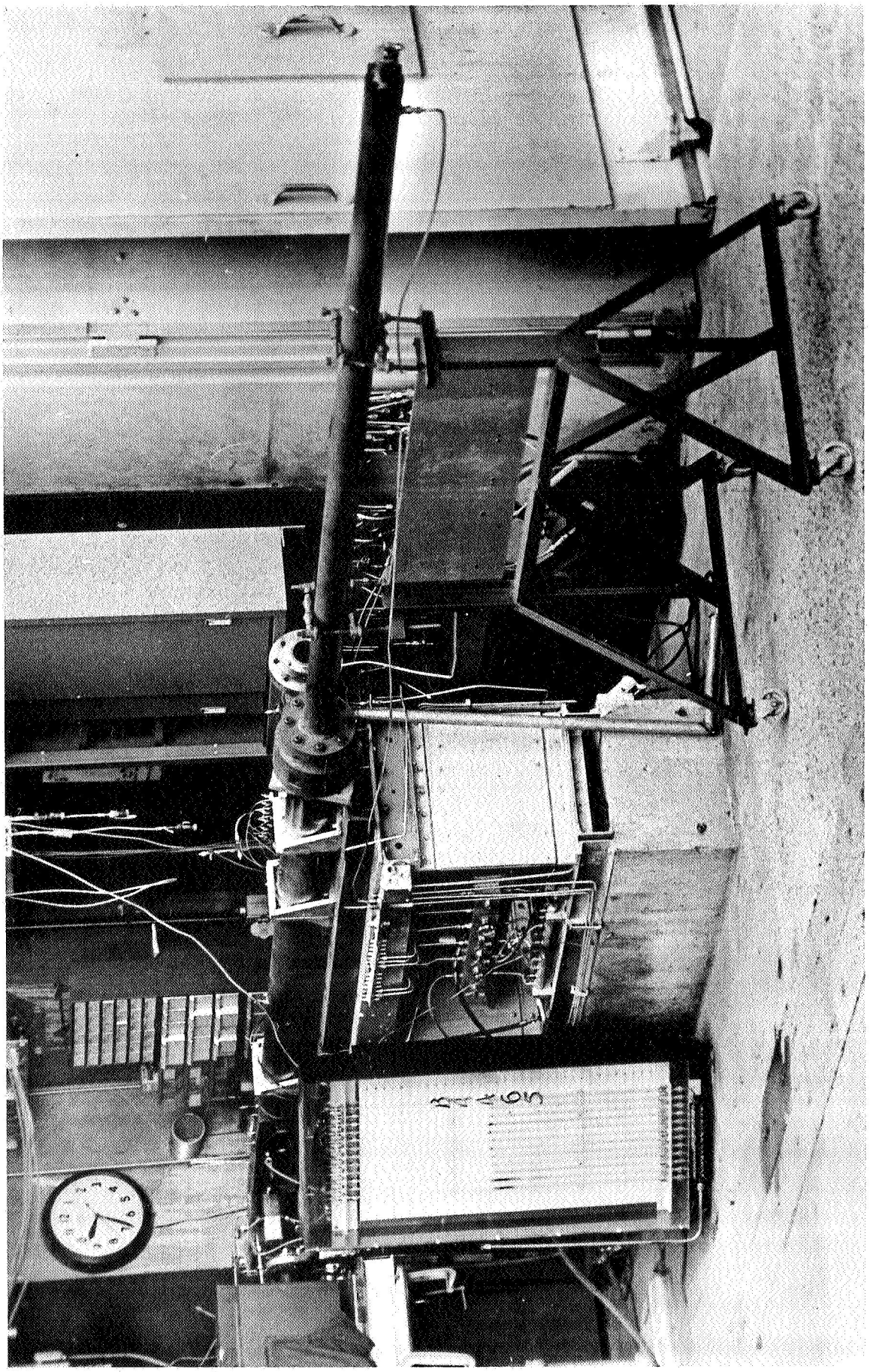

Rocket motor, shock tube assembly

Figure 12

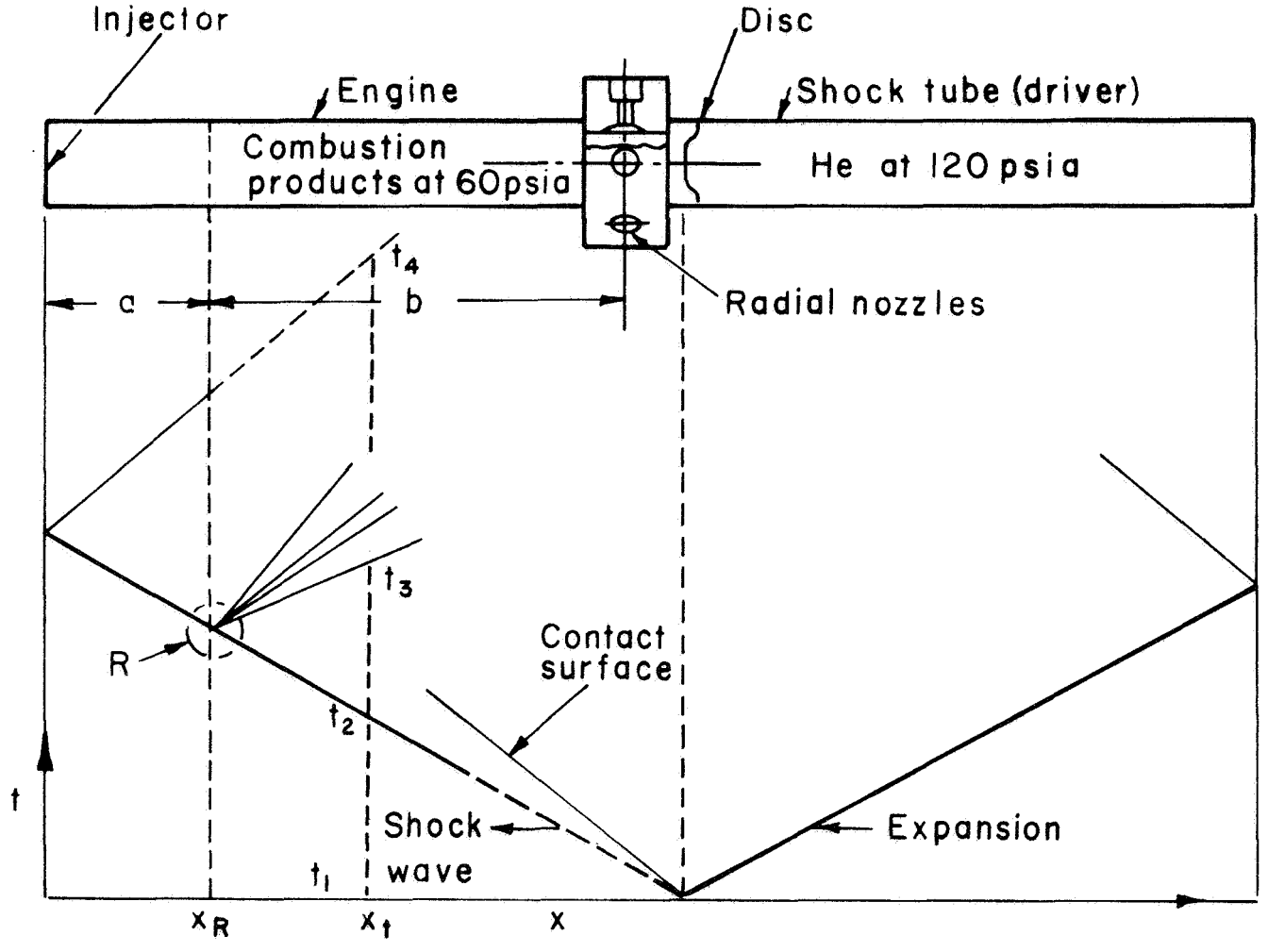

Characteristic shock history

Figure 13

(e.g., in zone "b") the effect of combustion would still be recorded for $t \geqslant t_3$. Notice also that the front of the shock should stay unchanged until R is reached, i.e., for all transducers positioned at $x > x_R$. The above explains why the effect of combustion is first noticed in the tail of the step shock and not at its front. Therefore, it can be shown that all deviations from a step-shock shape are due to gas non-uniformity and fuel burning in the active combustion Region a.

The behavior just described was recorded by an array of piezoelectric transducers (6 were normally used) located at numerous axial locations in the chamber. Repeatability was first established by playing the traces back from the high frequency analog tape and comparing traces at the same axial location for a number of runs and for different transducers. An example is shown in Fig. 14. To arrive at a final averaged pressure-time history, the recorded signals were transmitted through an analog-digital converter and on to an automatic plotter. This allowed each trace to be carefully equalized based on the individual transducer calibration as well as providing additional freedom in the choice of amplitude scales. These typical results are shown in Figs.15 and 16. Since the most extreme pressure amplitude variations of the shock front were found to occur near the injector, in a number of tests all six transducers were tightly clustered in that region.

MASS-SOURCE DETERMINATION

Having experimentally determined $p=p(x,t)$, the unsteady mass-energy source ($Q=Q(x,t)$) and the other unsteady gas variables ($u=u(x,t)$, $\rho=\rho(x,t)$), were determined as follows:

First, the steady state ahead of the shock was determined by a technique which did not require any assumptions about the droplet drag and vaporization processes. Some of the results obtained by this technique were presented[11] at the 1969 ICRPG meeting and the technique itself is discussed in more detail in Reference 12.

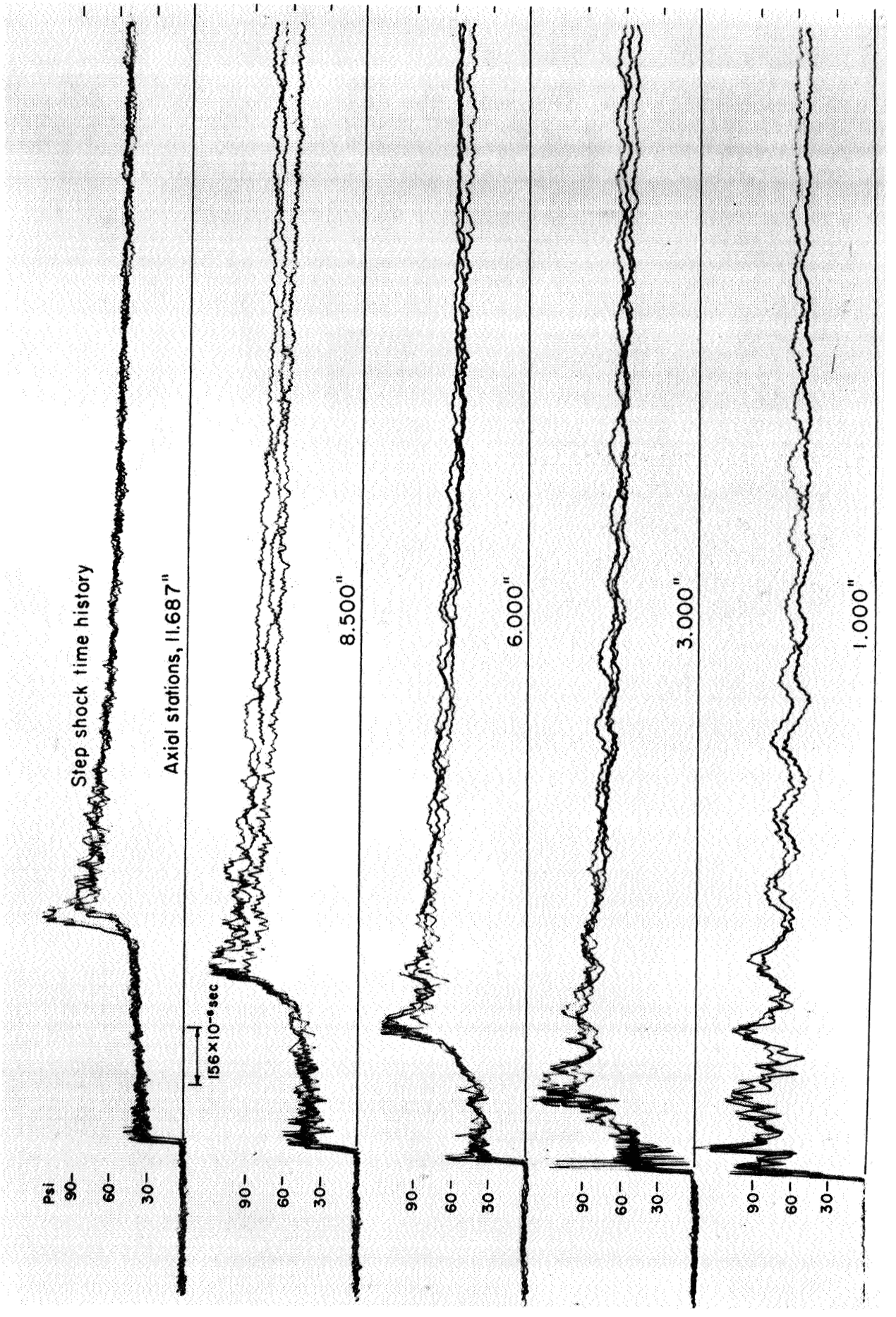
Step shock time history
Axial stations, 11.687"
156×10⁻⁶ sec
Psi
90
60
30
8.500"
6.000"
3.000"
1.000"

Figure 14

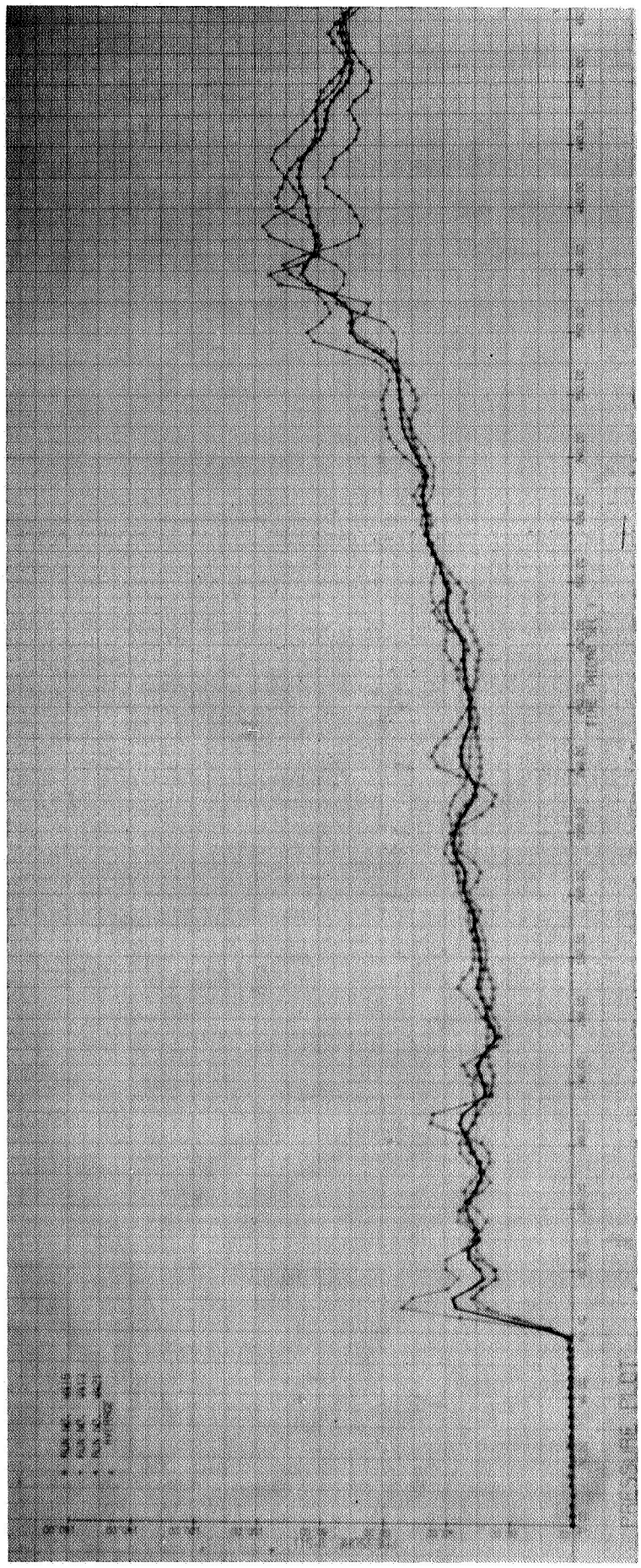

Static pressure vs time at 8.5" from injector

Figure 15

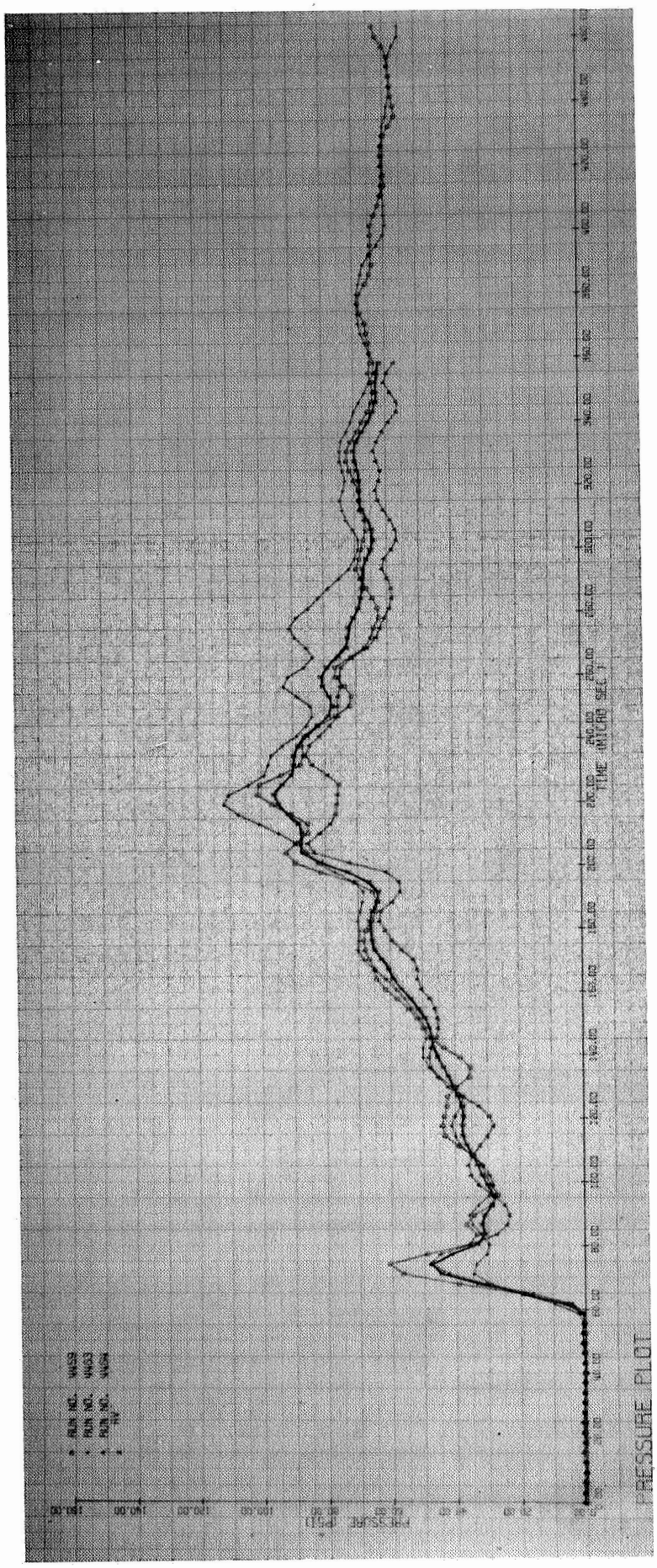

Static pressure vs time at 3" from injector

Figure 16

Second, the Rankine-Hugoniot equations were applied through the shock front thus determining the initial conditions for the unsteady flow which follows the shock.

Third, the previously given three unsteady, one-dimensional conservation equations were solved for $\rho = \rho(x,t)$, $u = u(x,t)$, and $Q = Q(x,t)$ by using the measured $p = p(x,t)$.

The measured $p=p(x,t)$ is given in dimensionless form in Fig. 17 and the computed $\rho = \rho(x,t)$, $u=u(x,t)$ and $Q=Q(x,t)$ are given in Figures 18, 19 and 20 respectively. It is important to notice that no use has been made of any drop drag and vaporization equations. The Q so determined can then be considered as an absolute mass-energy source that any unsteady drop burning model must reproduce to be acceptable. Notice also that the unsteady gas variables are now also known, so that the environment within which the unsteady burning of the drops occur is now completely known. The next step is to concentrate on various unsteady drop burning models and to see how they fit the already known unsteady gasdynamics environment. This step has not yet been completed.

CONCLUSIONS

1) The use of a step shock to probe for unsteady mass-energy sources in a liquid rocket motor was demonstrated. Careful control of the experiment as well as repeating the test conditions with replacement transducers was necessary to firmly establish each datum point.

2) Use of the experimental data, together with a knowledge of the steady-state conditions and the shock relations, allows one to calculate the mass-energy source.

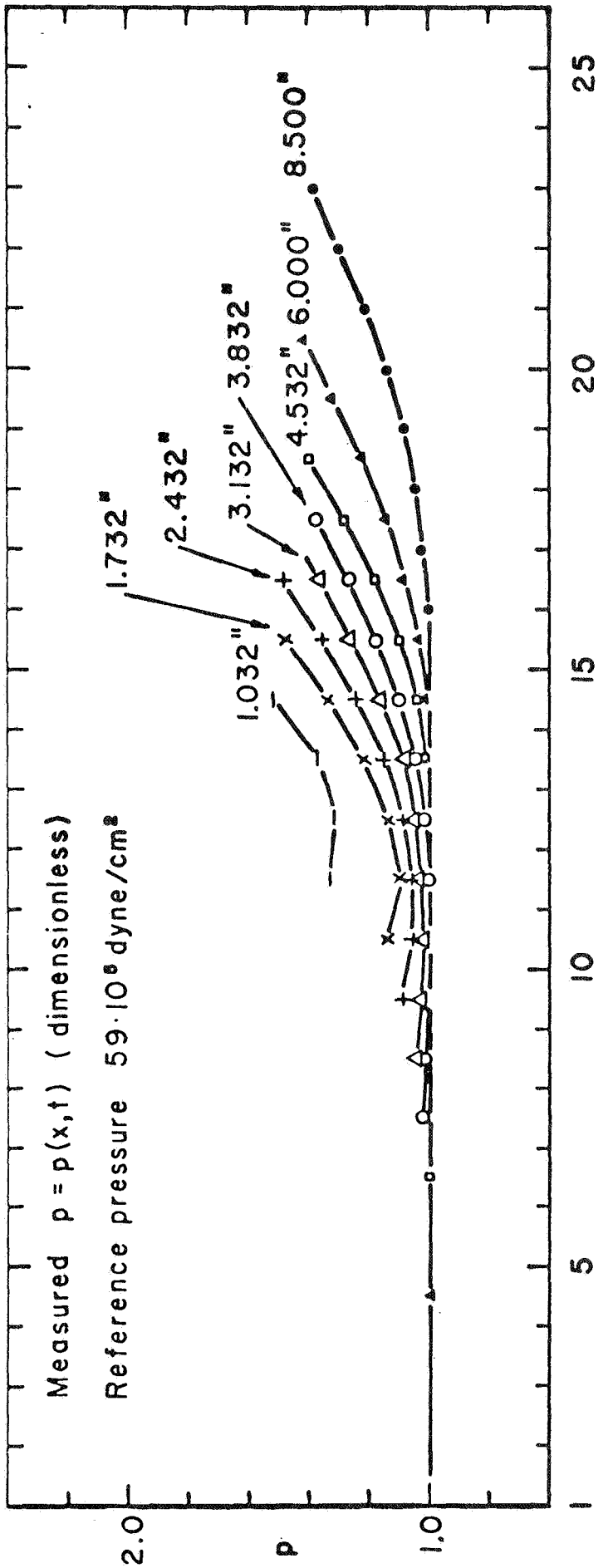
Measured p = p(x,t) (dimensionless)
Reference pressure 59·10⁶ dyne/cm²
p
2.0
1.0
1
5
10
15
20
25
t (1 cm = 20 microsec)
1.032"
1.732"
2.432"
3.132"
3.832"
4.532"
6.000"
8.500"

Figure 17

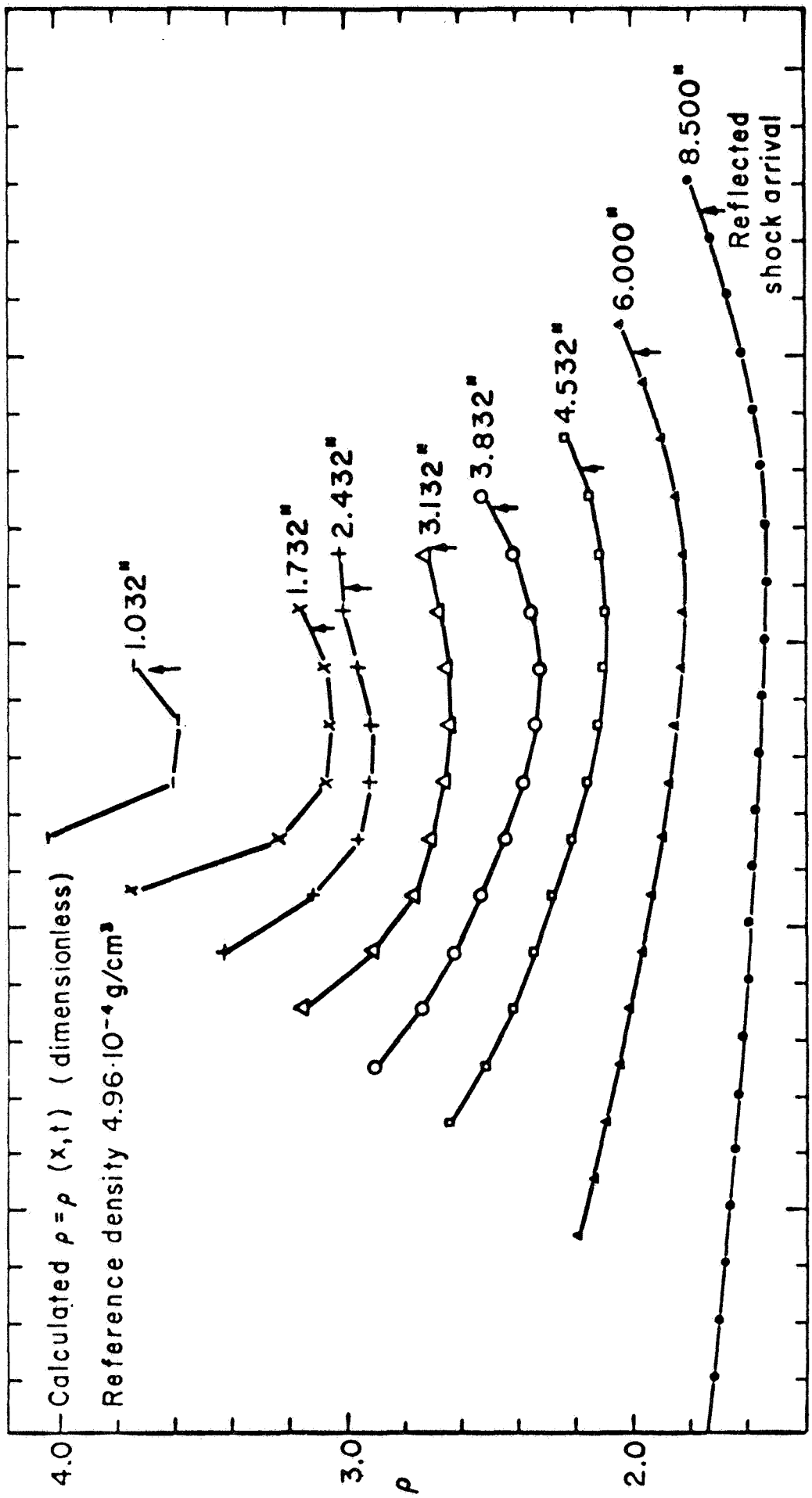

Figure 18

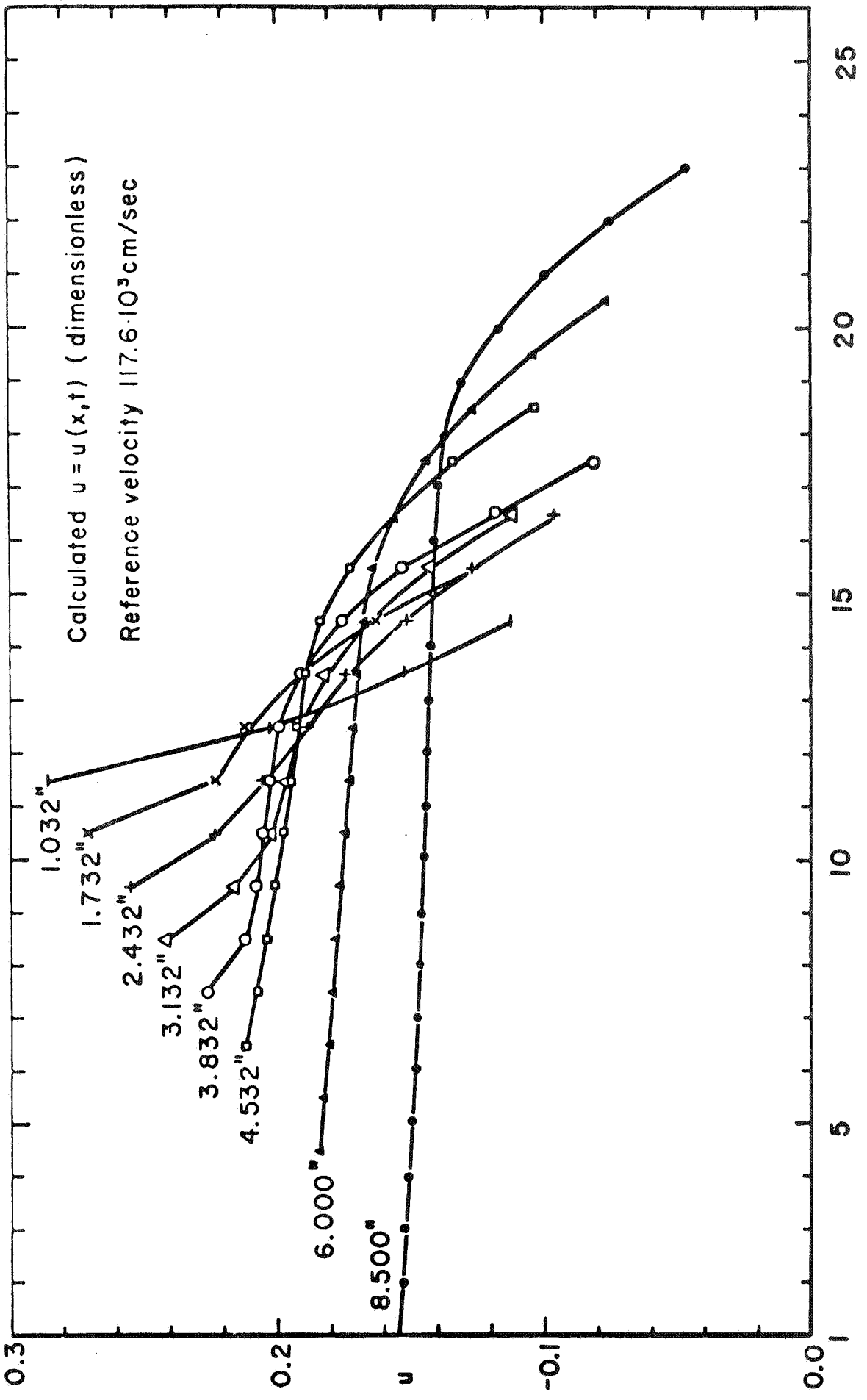
Calculated u = u(x,t) (dimensionless)
Reference velocity 117.6·10³cm/sec
1.032"
1.732"
2.432"
3.132"
3.832"
4.532"
6.000"
8.500"
0.3
0.2
u
-0.1
0.0
1
5
10
15
20
25
t (1cm = 20 microsec)

Figure 19

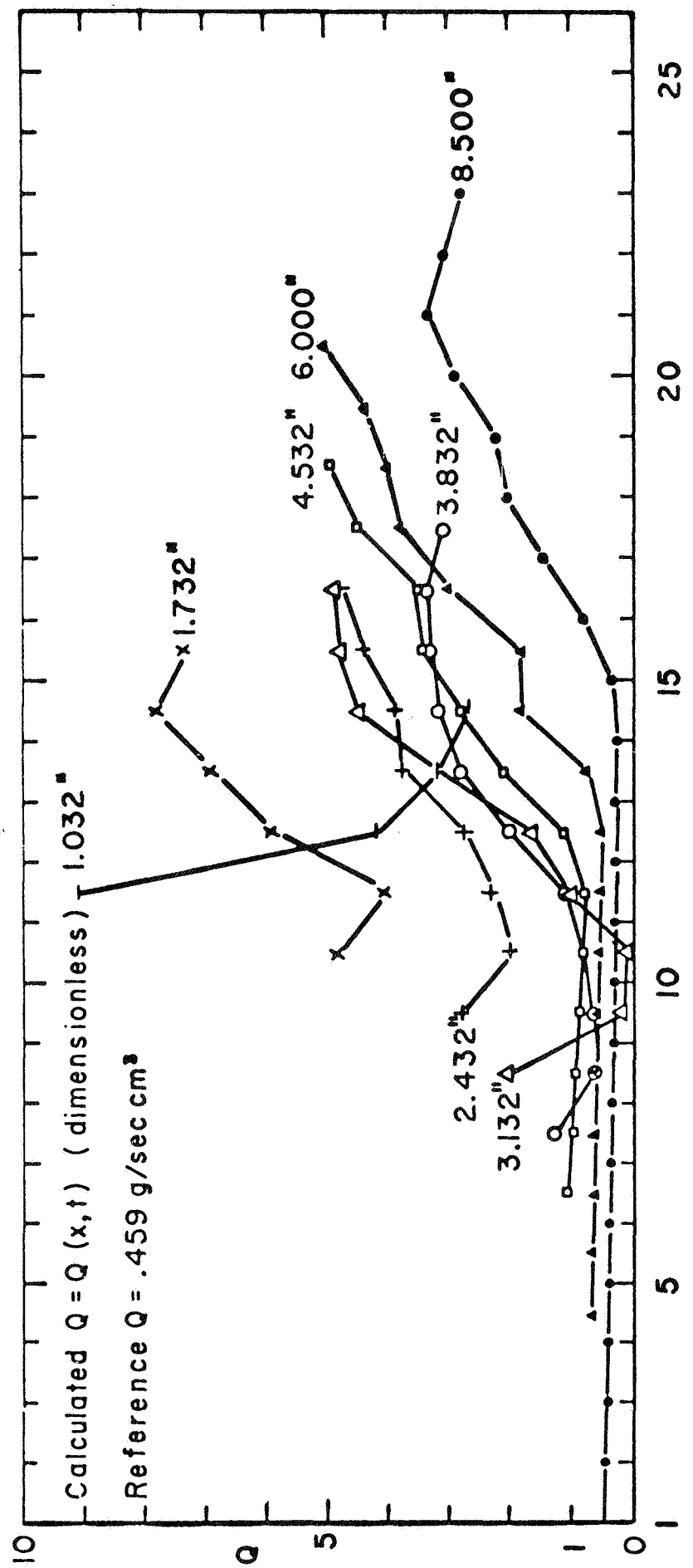
Calculated Q = Q (x, t) (dimensionless)
Reference Q = .459 g/sec cm³
Q
t (1 cm = 20 microsec)
1.032"
1.732"
2.432"
3.132"
3.832"
4.532"
6.000"
8.500"
10
5
1
0
1
5
10
15
20
25

Figure 20

V. THE EFFECT OF EXTERNAL PERIODIC DISTURBANCES ON AXISYMMETRIC WAKE DIFFUSION FLAMES

INTRODUCTION

In the study of combustion instability in liquid propellant rocket motors, it has been proposed that the mixing and burning of fuel and oxidizer either in the wake formed by the oxidizer-rich gas stream behind the fuel droplets or in the shear layer between adjacent fuel-rich and oxidizer-rich streams could provide the energy feedback necessary to drive high frequency oscillations in the combustion chamber.[13][14] Interactions of acoustic fields as well as finite amplitude oscillations with boundary layers, jets and wakes have been previously reported in the literature.[8][15][16] In those studies it has been shown that the interaction of the oscillations with the mean flow field may lead to earlier transition to turbulence, increased rates of heat transfer and other linear and nonlinear phenomena.

In the present investigation, the effect of finite amplitude periodic disturbances, imposed at the boundaries of axisymmetric jet diffusion flames has been studied. The interaction of the external oscillations with the flow field causes nonlinear changes in the mean flow structure resulting in an increased burning rate of the fuel per unit volume of the flame. A marked reduction of the mean flame length and flattening of the mean temperature distributions takes place. The proposed procedure for measuring the burning rate perturbation due to the oscillations is also presented.

EXPERIMENTAL APPARATUS AND PROCEDURE

A choked stream of natural grade propane is exhausted as an axisymmetric jet of 1/2" diameter into a glass chamber (10" diameter, open at one end) and ignited by a torch (see Fig. 21). A uniform velocity distribution of about 3 ft/sec is established at the burner outlet. An oscillating air stream flowing at a mean velocity of 1 ft/sec around the propane jet is introduced into the 10-inch diameter chamber via a system

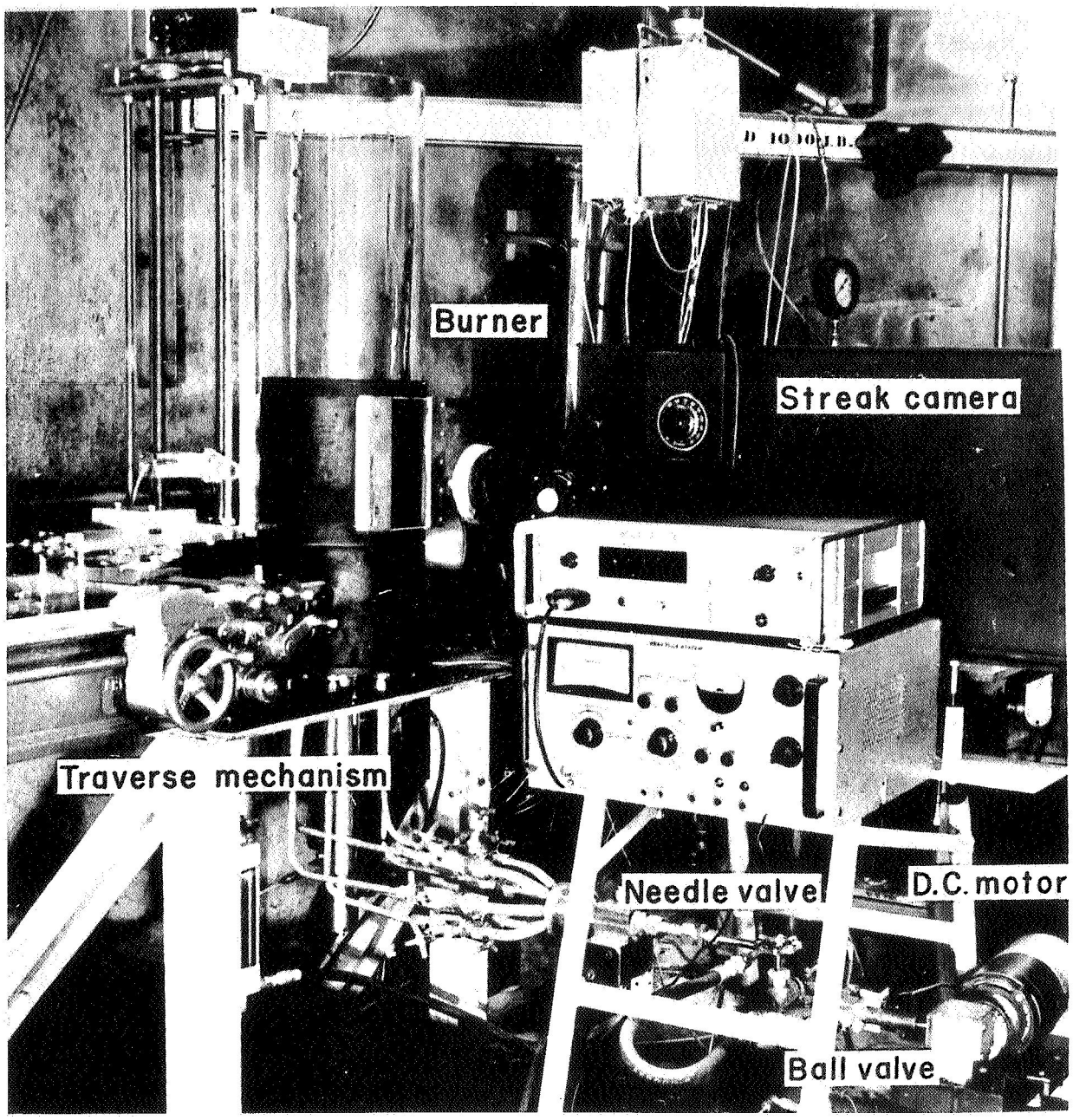

Experimental apparatus

Figure 21

which consists of a needle valve mounted in parallel with a ball valve rotated by a geared down variable speed motor. The frequency of oscillations is controlled by the motor speed while the amplitude is varied by altering the relative amounts of air passing through the needle-ball valve system.

Measurements of temperature distributions in the oscillating flames have been made using .003" Pt-Pt 10% Rh bare thermocouples and .0015" Pt. 30% Rh-Pt 6% Rh bare and coated thermocouples. The temperature data was corrected for radiation losses. Velocity measurements were made using a 1/16" dia. pitot-static tube and a heat flux probe. The heat flux sensor consists of a nitrogen-or water-cooled gold-coated quartz tube (.006" o.d., .004" i.d.) with a .05" long Pt film as the sensitive area. For the cold flows a .00015" tungsten hot wire was used. Radial and axial traverses of the oscillating flames were conducted at four frequencies (f = 2, 6 1/4, 15, 25 Hz) and two different amplitudes of the external flow oscillations as well as in steady state. Intensive measurements necessary to calculate the burning rate were also carried out at one axial station (x/D = 4). The experimental data was recorded on tapes, and reduced by a high speed computer using an A/D converter. Average and rms values of the fluctuating velocities and temperatures were calculated and plotted at various points.

EXPERIMENTAL RESULTS AND DISCUSSION

The effects of the external unsteady motion on the mean structure of the flame is shown in Figs.22 and 23. The oscillations cause a shortening and corresponding widening of the oscillating flame as compared to the steady state. The shadowgraph pictures suggest that the external oscillations interacted with the flame in the laminar flow region close to the burner outlet. At 15 Hz the oscillations cause a symmetric widening of the flame field and disruption of the potential core region which consists mainly of gaseous fuel. The effects

Steady-state flame

Oscillating flame
f=15Hz Amp=25%

Oscillating flame
f=15Hz Amp=50%

Shadowgraphs of oscillating flames
($\frac{1}{2}$" Burner)

Figure 22

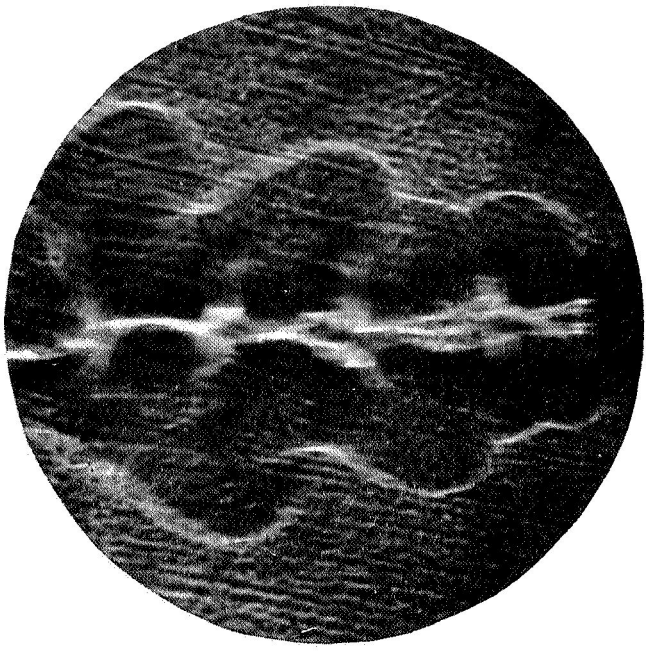

Oscillating flame
f=44 Hz Amp=50%

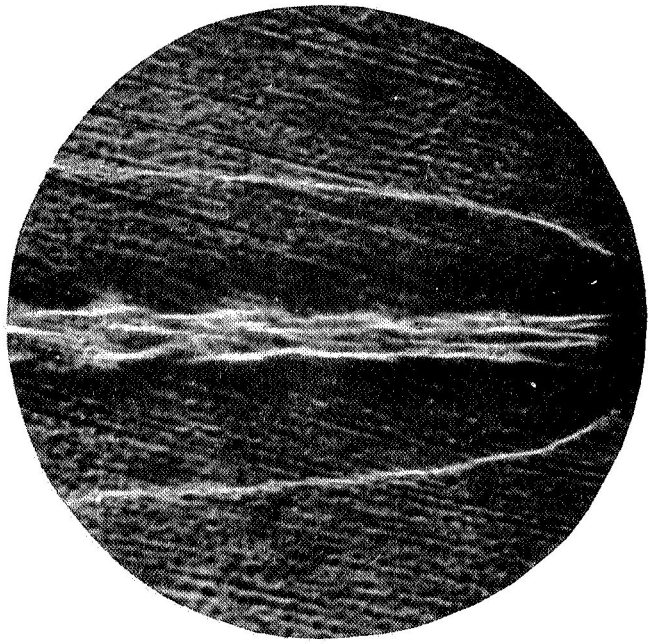

Oscillating flame
f=44 Hz Amp=25%

Shadowgraphs of oscillating flames
($\frac{1}{2}$"Burner)

Figure 23

increase with the amplitude of the oscillations. The interaction of the external oscillations is also frequency dependent. Experimentally the maximum disruption occurs at 15 Hz. The effects shown diminish with increasing frequency as shown by the 44 Hz shadowgraphs. The same decrease is witnessed at frequencies below 15 Hz.

Figure 24 shows the variation of the temperature on the jet axis under steady and oscillatory conditions. The increased mixing and intensification of the burning due to the oscillations is again seen. Higher temperatures and shorter potential core regions are associated with increased amplitudes of the external oscillations.

The maximum value of the rms temperature fluctuation is plotted as a function of the axial position in Fig.25. It is seen that an amplification of the temperature oscillation in the flame occurs between 4 and 6 diameters downstream of the burner outlet. A decay of the rms values followed by an increase of amplitude due to turbulence occurs further downstream. The figure also suggests that the onset of turbulence in flames may be expedited by large amplitude external oscillations.

The measurements in Figs.24 and 25 were carried out using a bare .003" Pt 10% Rh thermocouple. Due to the possibility of catalytic action at the thermocouple, the actual numbers in these figures may not be reliable but the indicated trends would be expected to be true.

The primary quantity of interest is the burning rate perturbation due to the interaction of the oscillations and the jet flow field. To determine the instantaneous burning rate in the jet diffusion flame the following parameters have to be measured

(i) the instantaneous flame position from which one can calculate the velocity of the flame surface $\vec{v}_{flame}$.

(ii) the gas density ρ, the gas streaming velocity $\vec{v}$ and the fuel concentration Y_F at the flame surface.

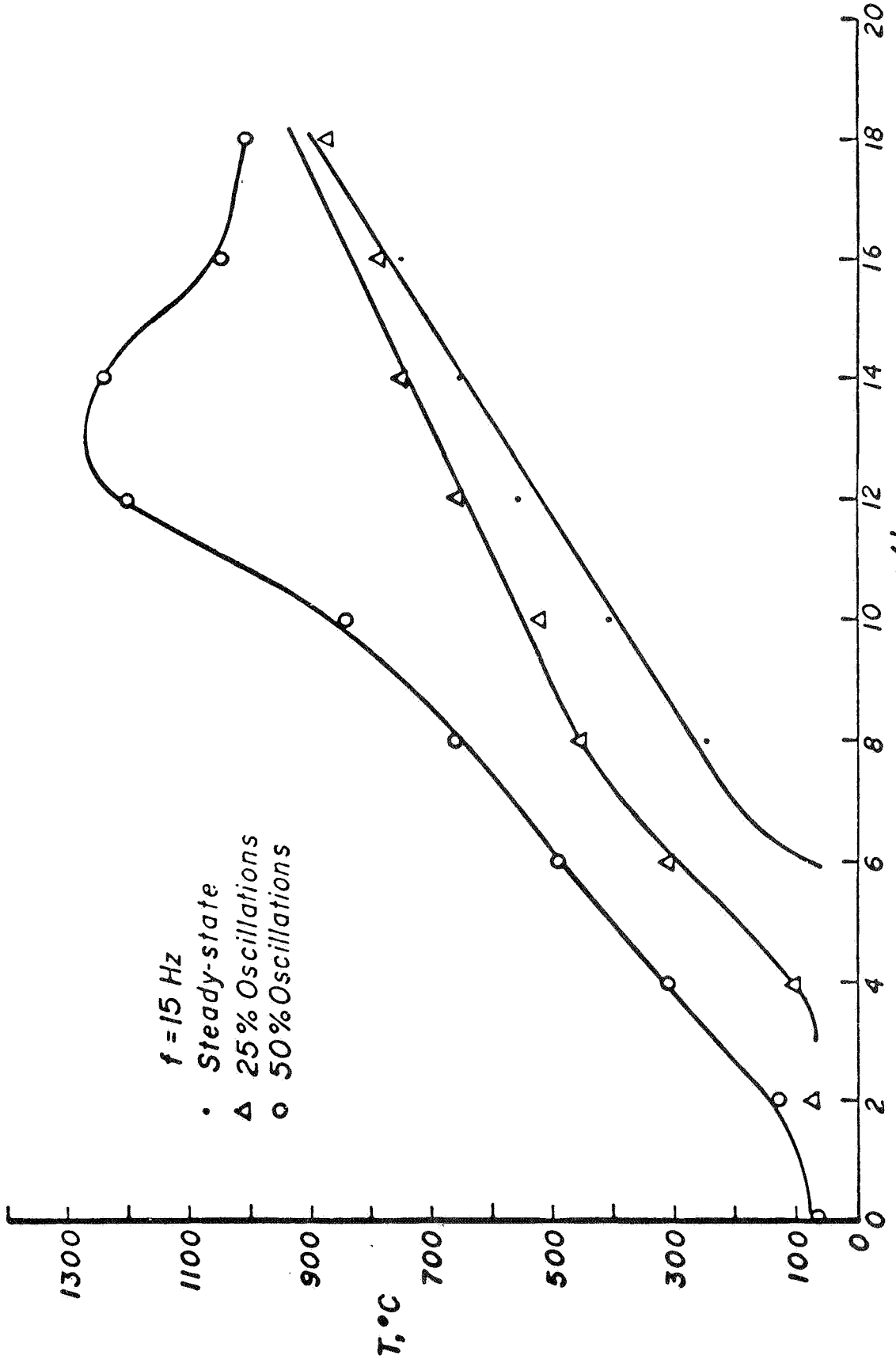

Variation of temperature on the flame axis

Figure 24

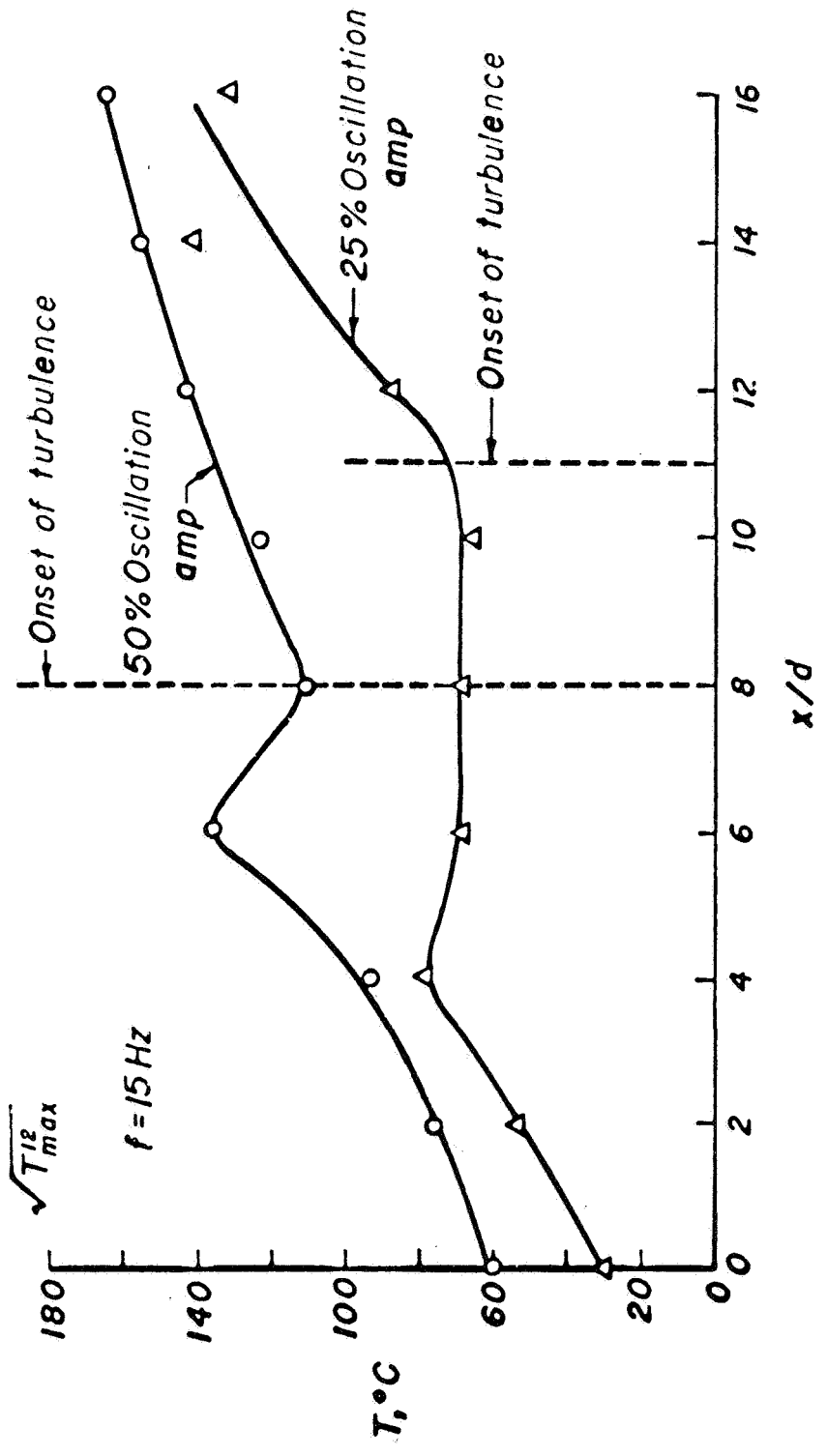

Variation of maximum value of RMS temperature fluctuation along the flame axis

Figure 25

Then the instantaneous mass burning rate

$$\dot{m}_b = \rho \, (\vec{v}_{rel} \cdot \vec{n}) \quad Y_F \Big|_{\text{flame front}}$$

where

$$\vec{v}_{rel} = \vec{v}_F - \vec{v}_{flame}$$

$$\vec{v}_F = \vec{v} + \vec{V}_F$$

$\vec{V}_F$ is the fuel diffusion velocity

$\vec{v}_{rel}$ is the fuel flow velocity relative to the flame front.

The gas density determination requires accurate measurements of the local gas temperature and pressure. Figure 26 shows detailed temperature profiles in the flame region in steady state at the axial station x/D = 4. The major effect of the coating is on the oxidation reactions on the outer edge of the flame, the coated thermocouple reading as much as 300°C lower than the bare thermocouple. On the fuel side the pyrolysis reactions are not affected by the thermocouple and the temperature readings are virtually identical. All subsequent measurements are being taken with coated thermocouples. The accuracy of the temperatures is very important since it will influence the accuracy in the determination of both the gas velocity and the fuel concentration.

A radial temperature distribution at 4 diameters downstream of the burner outlet is shown in Fig. 27. The oscillations mainly result in the flattening of the average temperature profile and an increase in the spread of the thermal layer. Due to increased mixing, the maximum flame temperature is lower than the steady-state value, the effect being larger with increasing amplitude of the external oscillations.

The instantaneous flame position can be determined from streak photographs as well as by point-by-point temperature measurements. Figure 28 shows the results from the streak

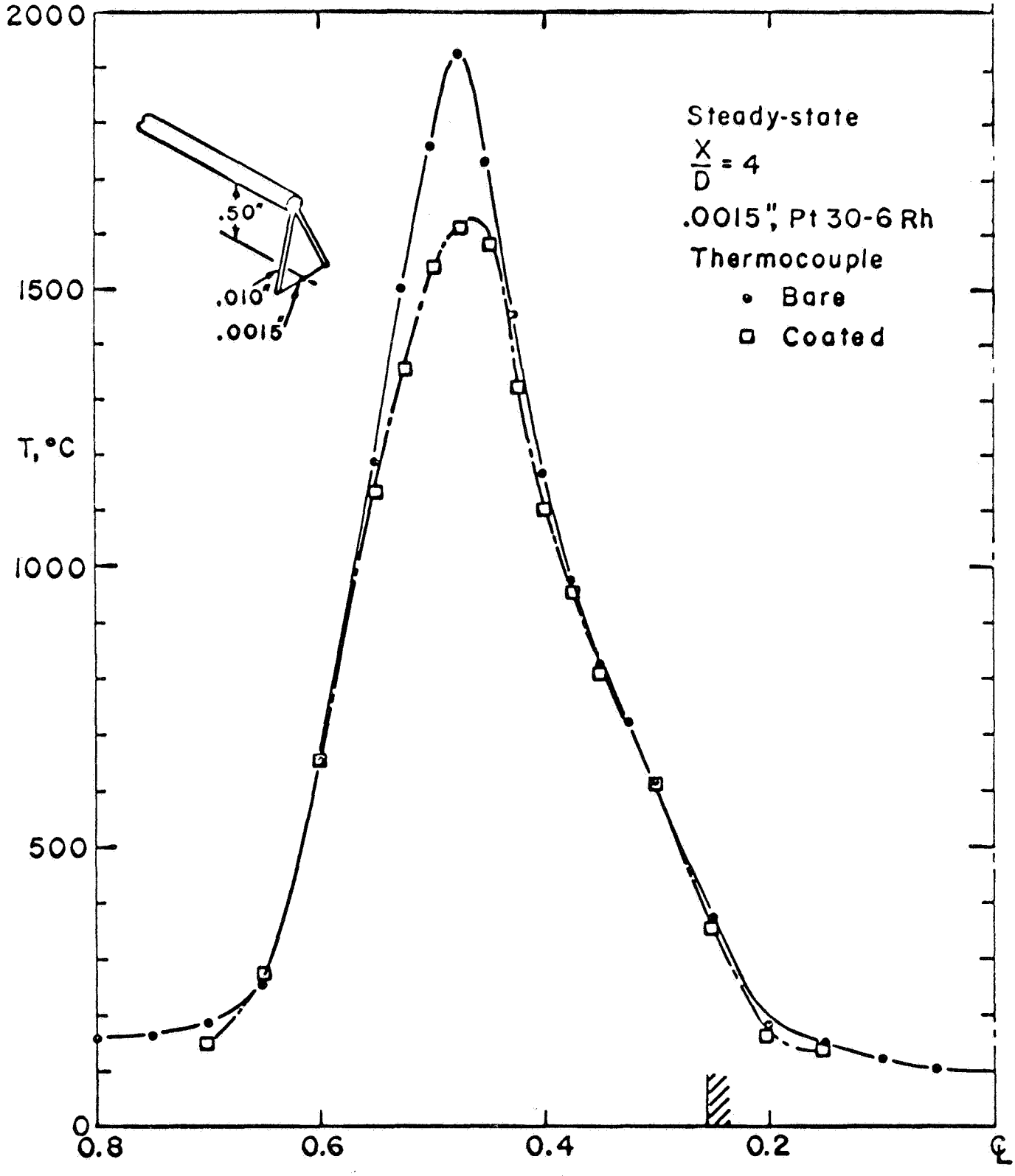

Radial temperature distribution, coated and bare thermocouples

Figure 26

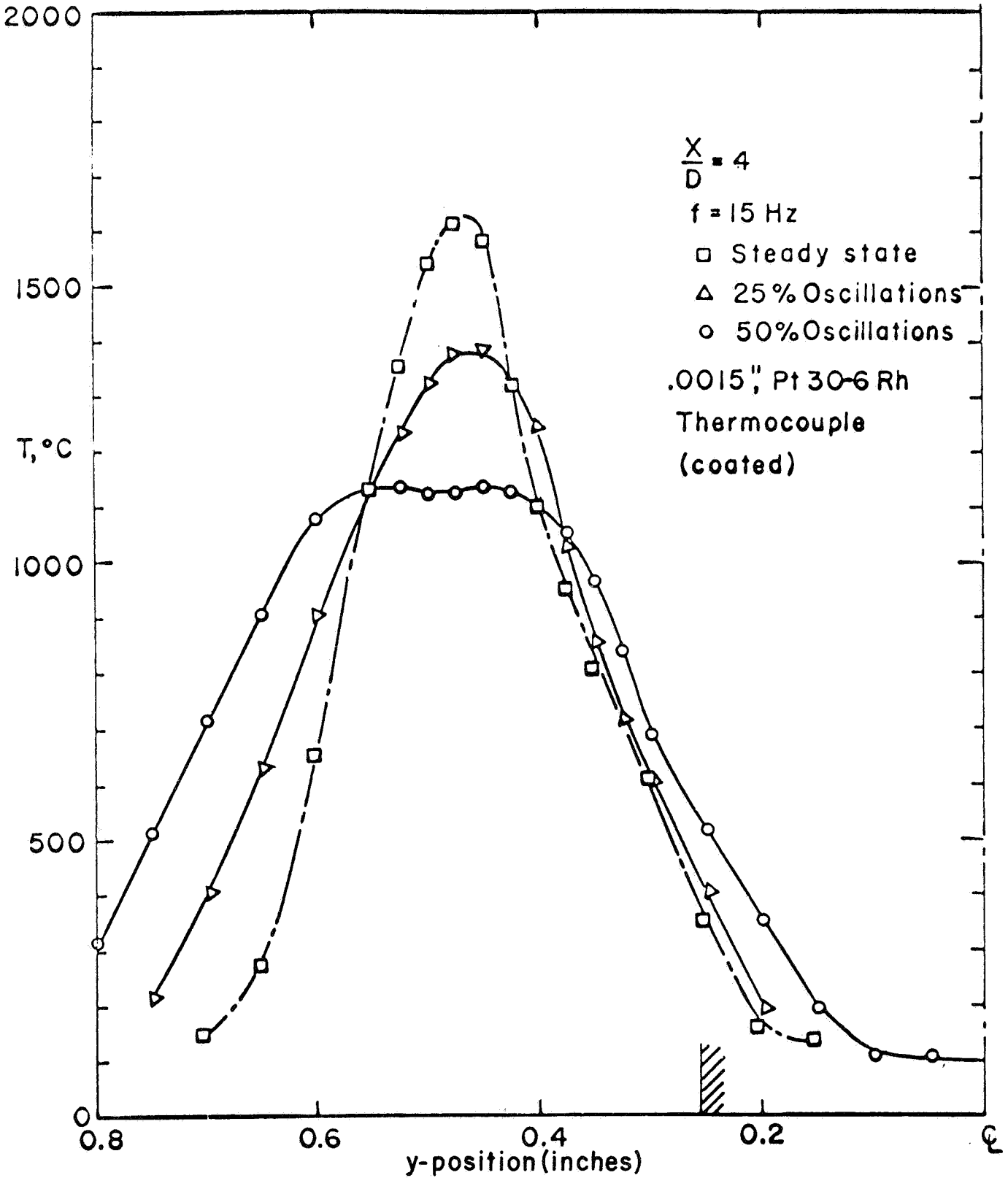

Figure 27

Radial temperature distribution
effect of oscillations

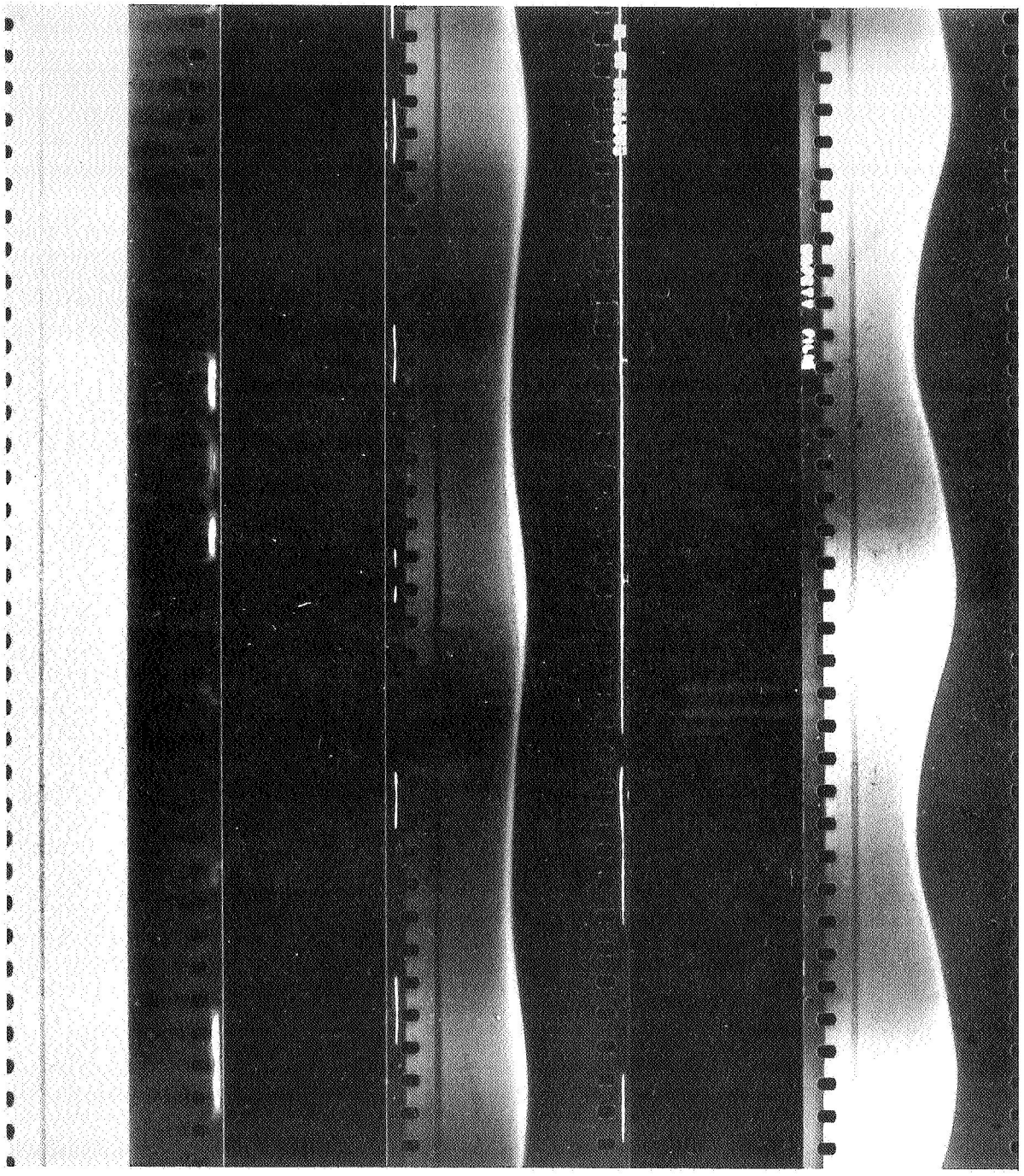

Steady 25% 50% Oscillations

Streak photographs of flame oscillations at $\frac{X}{D} = 4$

Figure 28

photographs. After calibrating the film, the limits of movement of the most luminous zone of the flame can be determined. In the steady state the separation between the peak temperature point and the edge of the flame as predicted by streak photographs is .029". Assuming this distance to remain the same in the oscillatory conditions, the instantaneous flame position can now be determined. In Fig.29 the predicted flame movement from streak photographs is compared to a peak temperature profile in the flame region. The change in the wave-shape of the thermocouple signal provides a fairly reliable indication of the limit of flame movement. The results from the streak photographs agree fairly well with the temperature measurements. Using a timing mark from the oscillation device the flame position can be plotted over a cycle of oscillation and the flame velocity can be calculated.

Preliminary velocity measurements in the flame are presented in Fig. 30. The pitot-static probe signal is read by a Datametrics variable capacitance transducer. Due to problems of coolant heating in the heat flux probe the measurements with that probe are reliable only in the outer region of the flame. The data with the two probes agrees fairly well. The velocity profile in a cold jet is also shown for comparison. The peak in the axial velocity in the region of the maximum temperature of the flame indicates the possibility of either buoyancy effects or pressure gradients in the flow field and these have to be investigated further.

The magnitude of the radial velocity is expected to be very small i.e., 5-10% of the axial velocity and it is proposed to calculate the radial velocity $\bar{v}$ by using the continuity equation and the experimentally measured values of the axial velocity u and the gas density ρ in the flow field.

The final parameter to be obtained is the fuel concentration at the flame surface. The theoretical procedure to calculate this parameter from the temperature measurements is outlined in the following subsection.

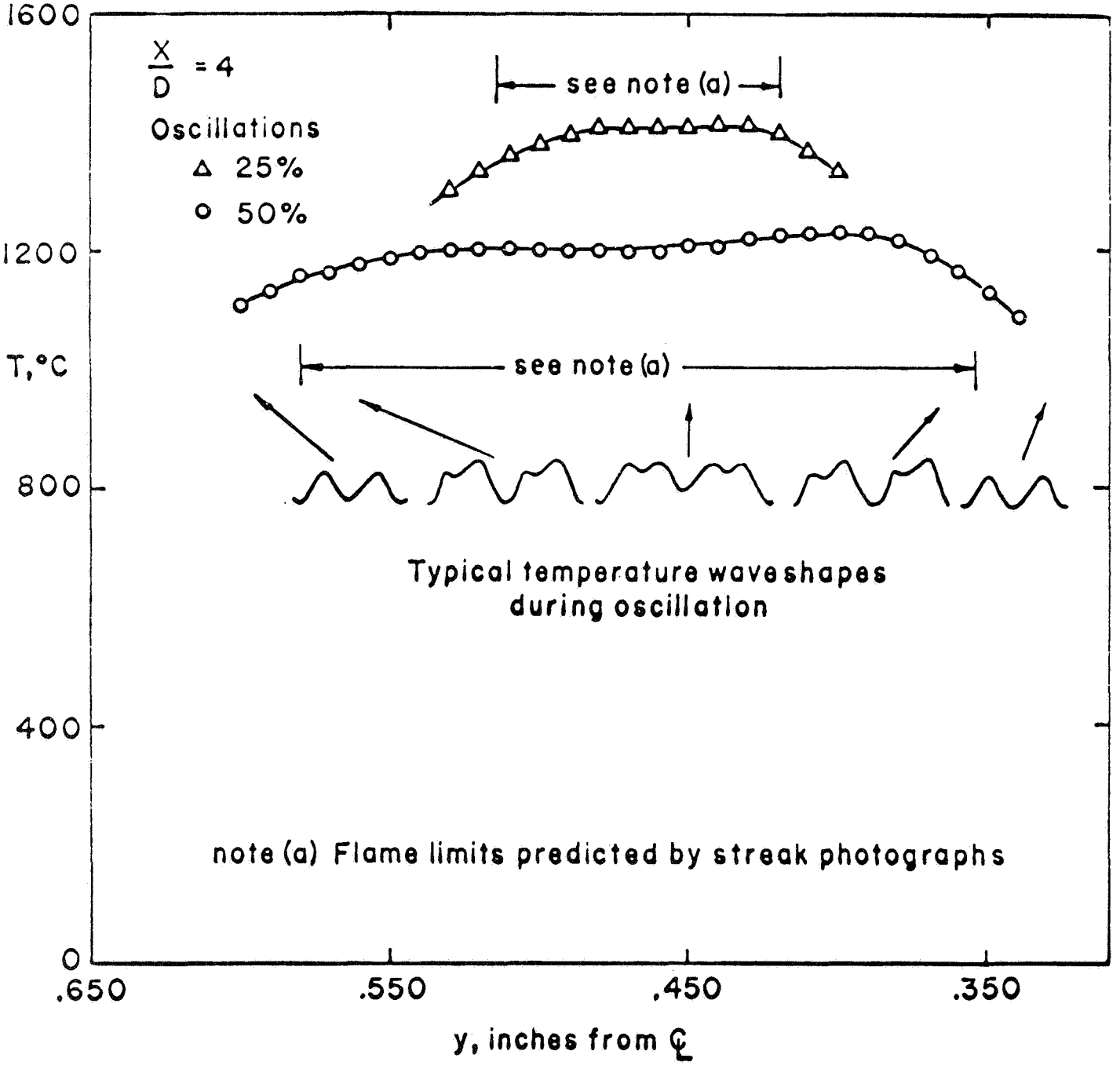

Peak temperature over region of flame oscillations

Figure 29

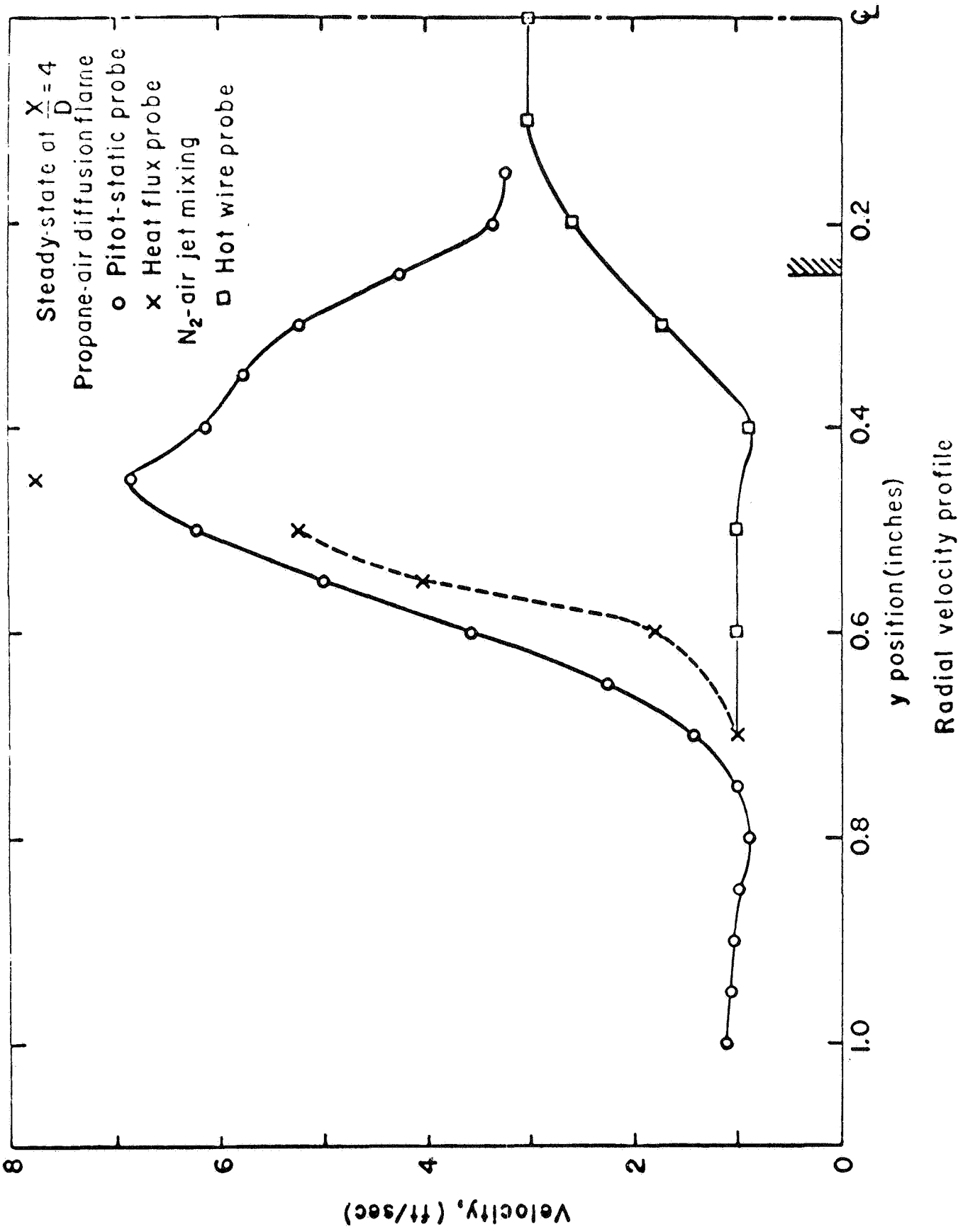
Steady-state at X/D = 4
Propane-air diffusion flame
o Pitot-static probe
× Heat flux probe
N2-air jet mixing
□ Hot wire probe
Velocity, (ft/sec)
0
2
4
6
8
0.2
0.4
0.6
0.8
1.0
y position (inches)
℄
Radial velocity profile

Figure 30

Determination of the Fuel Concentration

The theoretical analysis of the wake flow field shows that in the incompressible limit the equations for the Schvab-Zeldovich variables $\beta = \frac{h}{q^\circ} - \alpha_1$ and $\Gamma_i = Y_i/\omega_i \nu_i - \alpha_1$ become identical and therefore their solutions can be linearly related.

Considering the mixing region between the fuel region 1 and the oxidizer region 2 this gives -

$$\Gamma_i = \Gamma_{i,2} + \left(\Gamma_{i,1} - \Gamma_{i,2} \right) \frac{\beta - \beta_2}{\beta_1 - \beta_2}$$

where the subscripts indicate the boundary values in the 2 regions.

Substituting for the definitions of the Schvab-Zeldovich variables the following expression is obtained

$$Y_F = \left(Y_0 - Y_{0,2} \right) \frac{W_F \left(\nu_F'' - \nu_F' \right)}{W_0 \left(\nu_0'' - \nu_0' \right)} + \left[Y_{0,2} \frac{W_F \left(\nu_F'' - \nu_F' \right)}{W_0 \left(\nu_0'' - \nu_0' \right)} + Y_{F,1} \right] \left(\frac{T - T_2}{T_1 - T_2} \right)$$

Assuming the Burke-Schumann flame surface model, i.e., $Y_0 = 0$ in the fuel region, the fuel concentration can be calculated from the measured temperature distribution.

Also, then the fuel diffusion velocity $\vec{V}_F$ can be calculated by Fick's Law.

The instantaneous burning rate in the flame can thus be calculated. The major objective of the research program is to determine whether the burning rate perturbation due to the interaction between the oscillations and the diffusion flame flow-field is sufficient in magnitude and phase to drive the oscillations by itself or in combination with the response functions for other regions around the droplet.

CONCLUSIONS

1. The burning and mixing processes in jet diffusion flames interact with external periodic disturbances to a significant degree over a range of frequencies. The response is maximum at a certain critical frequency.

2. The interaction appears to take place mainly in the near region of the flame, ($<$ 8 diameters) where the period of oscillation and the diffusion time across the mixing layer are of the same order. The mean flame length decreases and the mean width increases.

3. A procedure for calculating the instantaneous burning rate has been outlined and preliminary measurements of some of the parameters have been achieved.

VI. CALCULATIONS ON ROCKET COMBUSTION INSTABILITY WITH A DROPLET EVAPORIZATION MODEL

INTRODUCTION

The emphasis in this research is to find a nonlinear combustion model to explain the occurrence of transverse combustion instability characterized by finite oscillation amplitudes and the possible appearance of shock waves. Clearly the oscillations cannot grow indefinitely but are limited by nonlinear effects in the given combustor environment. The linear or nonlinear behavior of oscillatory combustion depends fundamentally on the processes which, starting from the injected propellants, lead to the formation of combustion gases. It is indeed the effect of the oscillations on these processes and, hence, on the combustion rate itself, that supplies to the system an amount of feedback energy sufficient to balance the energy absorbed by dissipative and other damping processes and thus determines the final oscillation amplitude. In this presentation the purpose is to supply the latest results obtained with this model in regard to the nonlinear effects on pure transverse instability.

ANALYSIS

Under appropriate assumptions (Ref. 17), the combustion chamber equations between normalized variables are the following

$$\begin{aligned} &\rho_t + \nabla\cdot(\rho\,\underline{q}) = Q \\ &\rho\left[\underline{q}_t + (\underline{q}\cdot\nabla)\,\underline{q}\right] + \frac{1}{\gamma}\nabla p = Q\,(\underline{q}_\ell - \underline{q}) \\ &\frac{1}{\gamma}\,p_t + \nabla\cdot(p\,\underline{q}) + \frac{\gamma-1}{2}\left[(\rho\,q^2)_t + \nabla\cdot(\rho\,q^2\,\underline{q})\right] = Q \end{aligned} \qquad (1)$$

In the second equation the droplet drag has been neglected; consistently, we assume that the droplet motion is uniform with $\underline{q}_\ell = \underline{q}_{\ell i}$ = constant, provided the injection velocity is supposed insensitive to the chamber conditions. It is to be noticed that Eqs. (1) can be combined to give

$$\frac{1}{\gamma}\,p_t + p\nabla\cdot\underline{q} + \frac{1}{\gamma}\,\underline{q}\cdot\nabla p = Q\left[1 - \frac{\gamma-1}{2}\left(2\,\underline{q}_\ell\cdot\underline{q} + q^2\right)\right] \qquad (2)$$

which can be used instead of the continuity equation.

For the simplest droplet evaporation model the source strength Q coincides with the evaporation rate, which can be assumed to be proportional to the square root of the Reynolds number. The result can be written in the form

$$\frac{Q}{\mu/u_{\ell i}} = \frac{Q}{\beta} = -\frac{dV}{dt} = C\left(V \rho\, q_{rel}\right)^{1/2} \qquad (3)$$

where $\underline{q}_{\ell i}$ is assumed to have only the axial component $u_{\ell i}$, μ represents the injection rate per unit area, V is the volume of the droplet relative to its injection volume, and q_{rel} is the velocity of the droplet relative to the gas. The factor C will be assumed to be a constant determined by the steady-state conditions. However, in more sophisticated models it depends in an intricate fashion on the instantaneous conditions but not on the Reynolds number.

In order to study the possibility of transverse instability with this model, the geometry of the chamber (see Fig.31) is reduced to an annulus of very small thickness, so that the radial dependence can be disregarded and the quantities depend only on the time t, on the axial variable x and on the circumferential variable y. If, moreover, we concentrate for simplicity only on transverse spinning waves, we can assume a more restrictive dependence on x and on the combined variable θ = ft-y, where f represents the normalized frequency. Then Eq. (2) and the circumferential momentum equation can be written as

$$\begin{aligned} &\frac{1}{\gamma}(f-v)\,p_\theta + \frac{1}{\gamma}\,u\,p_x + p\,(u_x - v_\theta) = Q\left[1 - \frac{\gamma-1}{2}\left(2u_\ell u - u^2 - v^2\right)\right] \\ &(f-v)\,v_\theta + u\,v_x - (1/\gamma\rho)\,p_\theta = -(1/\rho)\,Q\,v \end{aligned} \qquad (4)$$

with u, v representing the axial and circumferential components of $\underline{q}$.

Each variable is now developed in a series of powers of a small parameter related to the combustion intensity, such as

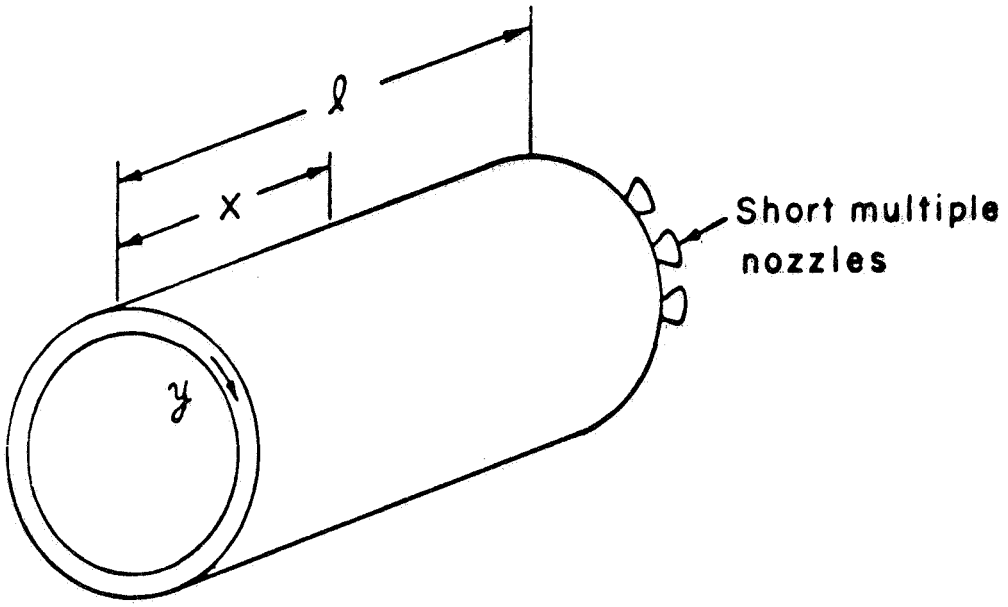

Thin annular combustion chamber

Figure 31

the injection rate per unit area μ . We have :

$$p = 1 + \mu p_1 + \mu^2 p_2 + \cdots ; \qquad v = \mu v_1 + \mu^2 v_2 + \cdots ;$$

$$u = \mu u_1 + \mu^2 u_2 + \cdots ; \qquad Q = \mu Q_1 + \mu^2 Q_2 + \cdots ;$$

The density can be written as $\rho = 1 + \mu (p_1/\gamma) + \cdots$, since it is easily shown that to the first order the transformations are isentropic if the combustion is conveniently distributed. Evidently, both u and Q must start with the first order term, since they must vanish for $\mu = 0$. If we choose the reference length, with respect to which x and y are normalized, to be the circumferential development of the chamber, we obtain for the frequency the development $f = 1 + \mu f_1 + \cdots$ Inserting the developments in Eqs. (4) we get the first order equations

$$\frac{1}{\gamma} p_{1\theta} + u_{1x} - v_{1\theta} = Q_1 \quad ; \quad v_{1\theta} - \frac{1}{\gamma} p_{1\theta} = 0 \tag{5}$$

and, hence,

$$u_{1x} = Q_1 \tag{6}$$

We observe that the solution of these equations can indeed be a spinning wave with p_1 and v_1 independent of x and $u_1 = \bar{u}_1$ or $u'_1 = 0$ (where $\bar{u}_1$ is the steady value and u'_1 is the perturbation) provided $Q'_1 = 0$, that is the combustion rate perturbation is of the second order with respect to its steady value $\bar{Q}_1 = \bar{u}_{1x}$. The solution of (5) is then given by $p_1/\gamma = v_1 = \varphi(\theta)$, φ being an arbitrary function. The second order equations obtained from Eqs. (4) are

$$\frac{1}{\gamma} p_{2\theta} + (f_1 - v_1) p_{1\theta} + u_{2x} - v_{2\theta} + p_1 (u_{1x} - v_{1\theta}) = Q_2$$

$$v_{2\theta} + (f_1 - v_1) v_{1\theta} - \frac{1}{\gamma} p_{2\theta} + \frac{1}{\gamma^2} p_1 p_{1\theta} = - Q_1 v_1$$

Adding the two equations and replacing the solution of Eqs. (4) we find

$$u_{2x} - \left[(\gamma+1)\varphi - 2 f_1 \right] \varphi_\theta + (\gamma+1) \bar{u}_{1x} \varphi = Q_2 \tag{7}$$

The value of f_1 can easily be obtained for a wave containing a shock from the shock velocity which, to first order, must be equal to the arithmetic mean between the wave velocities on the two sides of the shock (obtained from the sum of the corresponding particle and sound velocities). Hence, we get

$$f_1 = v_{1m} + \frac{\gamma-1}{2\gamma} p_{1m} = \frac{\gamma+1}{2} \varphi_m$$

the subscript m indicating the mean value at the shock. Finally, multiplying Eq. (6) by μ and Eq. (7) by μ^2 and adding, we can write the following equation between undeveloped variables

$$u_x = (\gamma+1)\left[(v-v_m) v_\theta - \bar{u}_x v\right] + Q$$

This equation can be integrated from the injector (x = o, u = o) to the nozzle entrance ($x = \ell$; $u = u_n$), where under the assumption of very short (multiple) nozzle, the Mach number must remain constant so that to second order accuracy

$$u_n = \bar{u}_n \left(1 + \frac{\gamma-1}{2\gamma} p_1\right) = \bar{u}_n \left(1 + \frac{\gamma-1}{2} v\right)$$

The result is

$$(\gamma+1)\ell\,(v-v_m) v_\theta = \bar{u}_n \left(1 + \frac{3\gamma+1}{2} v\right) - \int_0^\ell Q(x,\theta)\, dx \qquad (8)$$

If Q is known in terms of v , Eq. (8) is an equation which can be used to find the wave shape $v(\theta)$.

It is to be observed that the conditions for the second order validity of Eq. (8) are that $|v| \ll 1$ and $|Q'| = |Q - \bar{Q}| \ll \bar{Q}$. Let us now examine the consequences of Eqs. (3). Here d/dt represents the substantial derivative following the droplet and can be replaced by $f\,\partial/\partial\theta + u_\ell\,\partial/\partial x$. Consistent with the accuracy of the above calculations we can replace $q_{rel}^{1/2}$ by $\left[(u_\ell - \bar{u})^2 + v^2\right]^{1/4}$ and $\rho^{1/2}$ by $1 + v/2$. The solution of the equation for V (with V = 1 at the injector) is

$$\left[V(x,\theta)\right]^{1/2} = 1 - \frac{C'}{2u_\ell} \int_0^x \left[1 + \frac{1}{2} v\left(\theta - f\,\frac{x-\xi}{u_\ell}\right)\right] \left\{\left[u_\ell - \bar{u}(\xi)\right]^2 + v^2\left(\theta - f\,\frac{x-\xi}{u_\ell}\right)\right\}^{1/4} d\xi \qquad (9)$$

and hence we obtain

$$Q(x,\theta) = \beta C \left[1 + \frac{1}{2} v(\theta)\right] \left\{ \left[u_\ell - \bar{u}(x)\right]^2 + v^2(\theta) \right\}^{1/4} \left[V(x,\theta)\right]^{1/2} \qquad (10)$$

for the integrand in the last term of Eq. (8). The equation for v is now entirely defined for assigned values of C, $\bar{u}_n$, u_ℓ, γ and ℓ. It must be observed that it applies to the case of shock-type waves, and v_m represents the mean value at the shock with the frequency $f = 1 + \frac{\gamma+1}{2} v_m$. For shockless waves, of course, v_m is meaningless, but f is still meaningful, and v_m should be simply replaced by $\left(\frac{2}{\gamma+1}\right)(f-1)$. In this case instead of the unknown v_m to be determined simultaneously with the solution $v(\theta)$, we will have the unknown frequency f to be determined also in the same time as the solution $v(\theta)$. Of course, the same Eqs. (3) hold for the steady conditions, with $v = o$, $q_{rel} = |u_\ell - \bar{u}|$, and $\bar{Q} = \bar{u}_x$. From these equations one obtains the relation

$$\bar{u} = \beta u_\ell (1 - \bar{V}) = \bar{u}_n (1 - V)$$

and the distribution $\bar{u}(x)$ to be inserted in the expression above. Observe that $\beta = \bar{u}_n / u_\ell$ is of O(1) since the injection and the nozzle entrance velocity are generally of comparable magnitudes. Hence, we must distinguish three cases. For $\beta < 1$ we obtain the distribution from

$$1 - \frac{\bar{u}(x)}{u_\ell} = (1-\beta)\, Ch^2 K \left(1 - \frac{x}{b}\right)$$

where we have defined

$$K = \frac{1}{2} \ln \left| \frac{\beta^{1/2} + 1}{\beta^{1/2} - 1} \right| = \frac{C \beta^{1/2}}{2 u_\ell^{1/2}} b \qquad (11)$$

Here b represents the steady-state length of the combustion zone, where the values $\bar{u} = \bar{u}_n$ and $V=0$ are reached first. It is related to the droplets lifetime τ by $b = \tau u_\ell$ In the other case, $\beta > 1$, we obtain

$$1 - \frac{\bar{u}(x)}{u_\ell} = (\beta - 1)\, Sh^2 \alpha \qquad \text{or:} \quad \frac{\bar{u}(x)}{u_\ell} - 1 = (\beta - 1) \sin^2 \alpha$$

where $\alpha > 0$ for the first and $\alpha < 0$ for the second, i.e.,

$$\alpha = K - \left(K + \frac{\pi}{2}\right) \frac{x}{b} \gtrless 0$$

Finally, the exceptional case $\beta = 1$ should be treated separately, but we shall disregard it.

In all cases, to be consistent, b must always be sufficiently smaller than ℓ so as to prevent unburned droplets from reaching the nozzle during oscillations. Then in the calculation of $\int_0^{\ell} Q(x,\theta)\,dx$ the integrand will vanish at a certain station prior to ℓ (but generally $\neq$ b) determined by the vanishing of V. After this station, V and Q must be taken zero.

Observe that if ℓ and b are of O(1), Eq. (14) shows that C must be of the same order as $u_\ell'^{1/2}$, that is, of $O(\mu^{1/2})$ according to our assumptions, and consistently with the fact that Q must be of $O(\mu)$ and V of O(1). It is then easily seen from Eq. (9) and (10) that, because $\left[(u_\ell-\bar{u})^2+v^2\right]^{1/4} - |u_\ell-\bar{u}|^{1/2}$ is of $O(\mu'^{1/2})$ like $|u_\ell-\bar{u}|^{1/2}$, $(V^{1/2}-\bar{V}^{1/2})$ is of O(1) like $\bar{V}^{1/2}$, and therefore $Q-\bar{Q}$ is of $O(\mu)$ like $\bar{Q}$. Hence, one of the two conditions for the validity of Eq. (8) is not satisfied. This only means that the assumption $p_{1x} = v_{1x} = u_1' = 0$ cannot be satisfied and that in reality even to first order the spinning wave cannot consist of purely transversal perturbations. Despite this mathematical inconsistency, it is thought that the integration of Eq. (8) can provide interesting information since it contains the essential features of the gasdynamical true process and of the purely evaporative combustion mechanism.

SOLUTION AND DISCUSSION OF RESULTS

The solution of the resulting nonlinear integrodifferential Eq. (8) gives the unsteady behavior for the transverse velocity. Such a solution has been found by a numerical method using an iteration procedure. The Eq. (8), after substitution of the last term in developed form, may be rewritten as follows:

$$(v-v_m)\,v_\theta = A + B\,v(\theta) - D\left[1+\frac{v(\theta)}{2}\right]M(\theta) \qquad (12)$$

where A,B, and D are constant and M(θ) is the integral term. If the R.H.S. of Eq. (12) is defined as g(θ), one obtains

$$v_\theta = \frac{g(\theta)}{v - v_m} \tag{13}$$

There is a singular point for $\theta=\theta^*$ such that $v = v_m$ and to have a physical meaning it must be :

$$g(\theta^*) = 0 \tag{14}$$

Integrating Eq. (13) over the period and considering that

$$v_m = \frac{v(0)+v(1)}{2} \tag{15}$$

we obtain

$$\int_0^1 g(\theta)\, d\theta = 0 \tag{16}$$

Integration of Eq. (13) yields the formal relation

$$\left[v(\theta) - v_m\right]^2 = \left[v(0) - v_m\right]^2 + 2\int_0^\theta g(\theta')\, d\theta' \tag{17}$$

Equation (17) may be considered as a quadratic relation for v(0) and, therefore, has two solutions. It may be readily seen that, in the case where a shock exists and v(1) = v(0), we must have

$$v(\theta) = v_m + \left\{\left[v(0) - v_m\right]^2 + 2\int_0^\theta g(\theta')\, d\theta'\right\}^{1/2} \tag{18a}$$

for $0 \le \theta \le \theta^*$

and

$$v(\theta) = v_m - \left\{\left[v(0) - v_m\right]^2 + 2\int_0^\theta g(\theta')\, d\theta'\right\}^{1/2} \quad \text{for } \theta^* \le \theta \le 1 \tag{18b}$$

At $\theta = \theta^*$, $v(\theta^*) = v_m$ and

$$\left\{\left[v(0) - v_m\right]^2 + 2\int_0^{\theta^*} g(\theta')\, d\theta'\right\}^{1/2} = 0 \tag{19}$$

Because we are only interested in real-valued solutions that are continuous at $\theta = \theta^*$, it must be that the radicand in Eq. (19) be a minimum (=0) at $\theta = \theta^*$. This is consistent with the fact that $g(\theta^*) = 0$. The iteration procedure used for the numerical solution begins with assuming $v(\theta) = v(0)+$

$+\phi(\theta)$ where $\phi(0) = 0$, a sawtooth profile was assumed. Use has been made of Eq. (16) to obtain v(0). Knowing v(0) and $\phi(\theta)$, $v(\theta)$ is immediately known and may be substituted into the R.H.S. of Eq. (18) and v_m is determined from Eq. (19). Equation (18) is then used to calculate a new $v(\theta)$. We are now able to find out a new $\phi(\theta)$ from

$$\phi(\theta) = v(\theta) - v(0) \tag{20}$$

and again use is made of Eq. (16) to obtain a new v(0), and so on, until the sequences for $v(\theta)$ and v_m converge. Results for $\beta<1$ and for $\beta>1$ are shown in Fig. 32 and Fig. 33 for different values of τ.

CONCLUSION AND REMARKS

Rather than seeking the general solution, we have restricted ourselves to the narrower objective of looking for periodic solutions in the circumferential variable y. These solutions were found to exist and are stable from a mathematical standpoint. The solutions are shock-type and represent the limiting cycle of unstable operation that is produced in a nonlinearly way.

The transverse velocity distributions shown in Fig. 32 and 33 indicate, that for a same β, as the droplet lifetime gets smaller and smaller, the shock amplitude reaches higher values.

Increasing the velocity of the gas at the nozzle entrance (with respect to a constant value of the liquid velocity which for convenience has been taken 0.1), and for constant droplet lifetimes, higher shock amplitudes result.

Before drawing any conclusion on the behalf of stable and unstable regions of operation, periodic behavior of the shock-type solution has to be found with respect to time and this is the purpose of this continuing investigation.

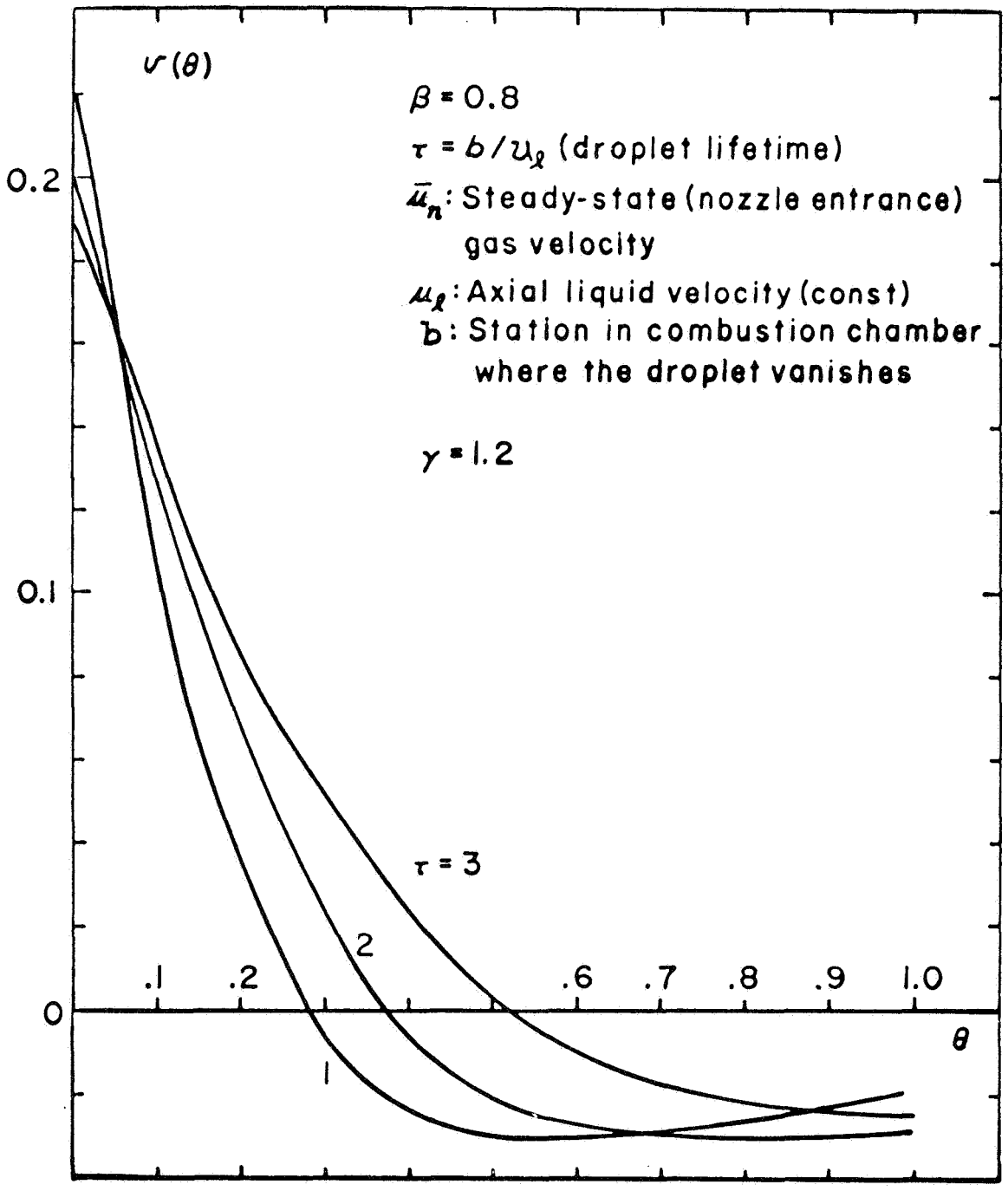

Shock-type transversal velocity distribution in a thin annular chamber

Figure 32

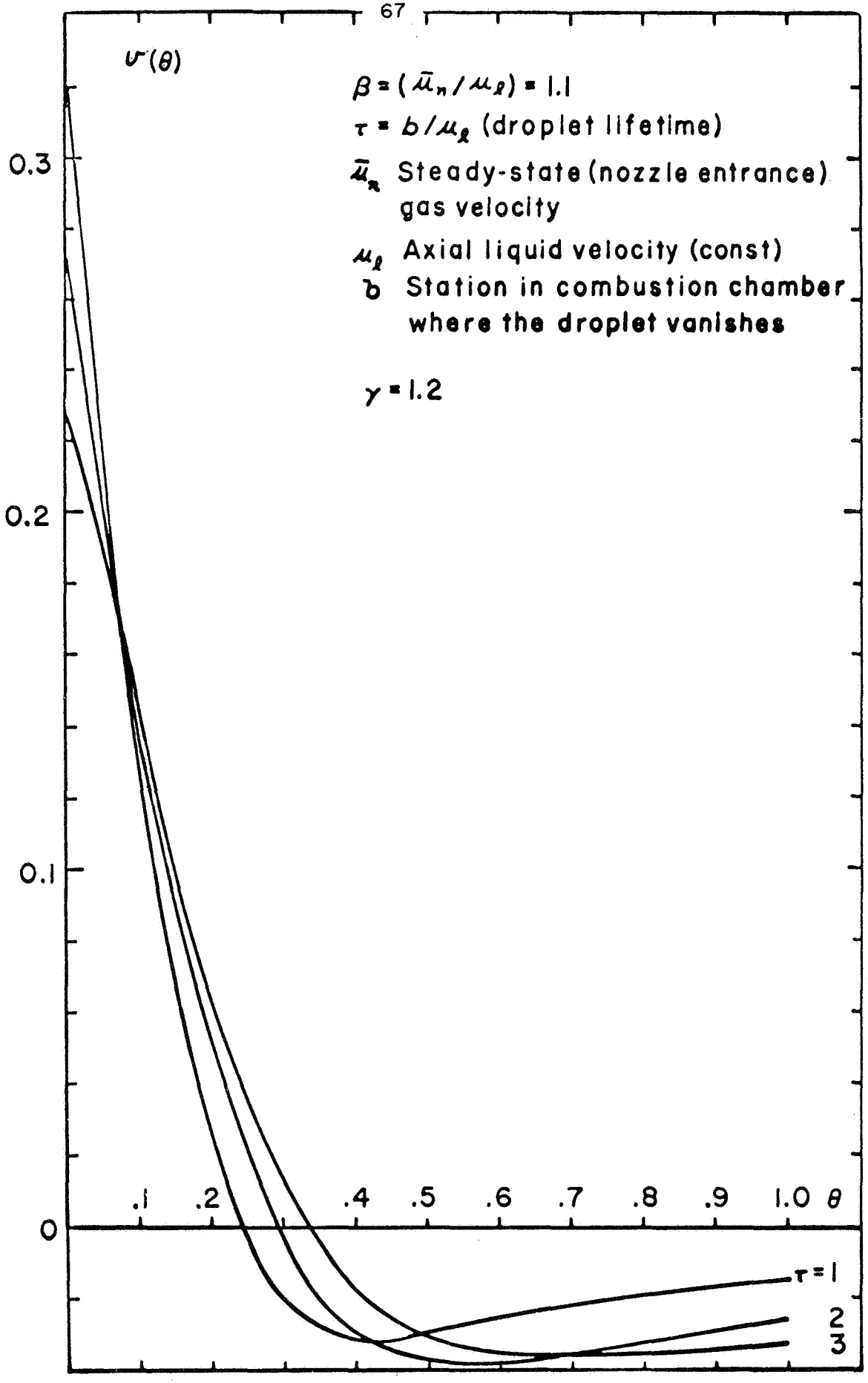

Shock-type transversal velocity distribution in a thin annular chamber

Figure 33

VII. HYDROGENATION ROCKET FEASIBILITY STUDIES

INTRODUCTION

The concept that launched this investigation into the possibilities of using hydrogenation as an energy source applicable to rocket propulsion was based on the previous work of Glassman(1965)[18]. The document outlined the theoretical advantages to using a bipropellant system of hydrogen and an acetylenic hydrocarbon. These advantages included high performance with the creation of products very conducive to afterburning; specifically, gaseous methane and hydrogen. Chamber characteristics in such a reaction were relatively low pressure and temperature.

The acetylenic hydrocarbon used in this particular investigation was methyl acetylene (C_3H_4). The rationale for this choice was safety, as the limits of flamability (percent fuel in air which will combust) and the sensitivity to shock were both much less than an alternative such as acetylene (C_2H_2).

Methyl acetylene (MA) is a monopropellant. In a thrust chamber pressurized to twenty atmospheres, it will decompose to the product's graphite (fine carbon particles) and hydrogen. The performance based on this mode of operation would be unattractive for propulsive applications. Calculations indicate that the specific impulse would be less than two hundred seconds. The addition of hydrogen, however, offers the possibility that the reaction will be forced to a hydrogenation of the unsaturated hydrocarbon. Ultimately only methane and hydrogen would then be formed as products. Equilibrium calculations reveal that under the influence of twenty atmospheres of chamber pressure, the following reaction marks this product limit:

$$C_3H_4 + 12\ H_2 \rightarrow 3CH_4 + 8\ H_2 \qquad (1600^{\circ}F)$$

Higher hydrocarbons would almost certainly be produced also, but their low equilibrium constants indicate their percentages would be small. For example, the equilibrium constant for ethene (C_2H_4) at 2250°F is 2.6×10^{-6} or four orders of magnitude smaller than that of methane. The ratio of twelve moles of hydrogen per mole of MA (or molar mixture ratio, mmr = 12) was arrived at as the completion ratio by an iterative product and temperature determination method.

High performance expectations were drawn from the proportionality $I_{sp} \sim (T/MW)^{\frac{1}{2}}$ where I_{sp} is the specific impulse, T is the chamber temperature, and MW is the average molecular weight of the products. Although the temperature is low in the monopropellant mode (no hydrogen added) and is depressed further by the hydrogen, the low molecular weights associated with a hydrogenation reaction more than compensate, resulting in a high specific impulse. In particular for the hydrogenation reaction as depicted above, a performance of over 350 sec. of impulse would be expected.

Applications of a successful hydrogenation system could include use as a first stage booster. Ambient oxygen could be utilized in the afterburning, creating a ram-jet type thruster. The materials required for such an application need not be of exotic nature due to the low pressure and temperature requirements. The basic simplicity of design, the possibility of reuse, and the large-quantity fuel price[20] would all aid in making such a rocket economically feasible.

TEST HISTORY

Prior to this period of investigation, some information had been obtained.[19] Temperature measurements during initial runs clearly confirmed the expected low chamber temperature. The monopropellant mode of operation produced the highest temperatures, but even these were below 2300°F. The addition of hydrogen reduced the chamber temperatures, as expected, to values below 2200°F. Temperature profiles along the chamber axis were also measured. The combustion chamber was

twelve inches long; a uniform temperature profile was established for more than three-quarters of this length. It was also found that the addition of hydrogen increased the performance of the rocket significantly above the monopropellant mode of operation. This initial addition of hydrogen occurred at low molar mixture ratios. It was not possible, however, to comment with certainty as to the composition of the exhaust products. It was shown that the increased performance could result from either of two mechanisms: (1) the hydrogenation reaction was proceeding, at least in part, yielding gaseous products of a low molecular weight; (2) the hydrogen was behaving as a low molecular weight working fluid for the methyl acetylene decomposition. Of course some combination of these two was possible. Before proceeding to higher mmr, it was decided to develop a gas sampling and analyzing technique to determine the composition of the exhaust products. It is toward this goal that the entire effort was directed.

SAMPLING

The technique of obtaining a gas sample has proven to be a delicate operation. Two prime requirements had to be met if a representative sample was to be captured: (1) the gas sample had to be quenched immediately to prevent further chemical reaction; (2) the entire sample system had to remain free from contaminants. The first of these requirements was met by use of a water-cooled probe. It was assembled from three, concentric tubes and a machined tip. All material was stainless steel. The overall dimensions were 30" x 1/2" O.D. The tip was machined to provide a nozzle entrance to the inner tube. This design provided gas dynamic cooling as well as metering. The outer two tubes provided the jacket for the cooling water flow. It was found that when plumbed to a city water supply, the probe reduced the sample gas temperature from chamber levels of 2200^{o}F to approximately 100^{o}F. The characteristic time for this cooling was of the order of

one millisecond. The second requirement was complicated by the presence of the fine, powdered carbon in the exhaust. The added requirement for remote operation increased the difficulties, e.g., the solenoid valves either failed to close properly, or plugged with carbon completely. As the system was finally operated, the sample was trapped in a helix of 1/4" stainless steel tubing by using two ball valves, operated simultaneously by a pneumatic piston. The design of the "sample bottle" eliminated dead zones in the gas flow. The gas samples were obtained at a pressure of 20 psig to inhibit contamination from the atmosphere. The actual samples were taken from the center of the combustion chamber just before the nozzle entrance. Chamber temperature was measured in the same radial plane. The flow was assumed to be chemically frozen in passing through the probe nozzle.

The analysis of the product sample was conducted with the Hewlett Packard 7620A Gas Chromatograph Analyzer (GCA). By affording a temperature programming capability, this GCA provides a higher resolution and sharpness of recorder peaks than the fixed-temperature type unit. The temperature program used in the product analysis was from $-86^{\circ}C$ to $120^{\circ}C$ with liquid nitrogen as the cooling agent. The column used was 12' x 1/8" O.D. stainless steel tubing packed with Parapak Q (mesh size 80/100). The sensing element in the equipment was a standard thermal conductivity cell with helium as the carrier gas.

The curves obtained represent the number and relative abundance of constituent gases. The extreme sharpness of these curves allows the use of peak height as the measure of abundance. The position of each gas peak and the height these peaks reached in a known concentration were obtained by analyzing a calibration gas under operating conditions identical to those at which the sample analysis was performed. In this way all the sample peaks have been quantitatively identified with the exception of a few higher hydrocarbons

(C_3, C_4) which represented only one or two percent of the sample.

RESULTS

The tests of the hydrogenation rocket indicated that an upper limit for mmr exists, which is well below the desired operating point of mmr = 12. Several attempts were made to inject hydrogen at levels corresponding to mmr > 4.3. In each case the decomposition reaction extinguished immediately. The same result occurred for either of two hydrogen injection schemes: (1) step input of hydrogen mass flow to a preset level; (2) ramp input of hydrogen mass flow from mmr = 0. One set of data indicated that the problem stemmed from excessively high injection velocities. However, that indication was shown to be false when attempts to sustain reaction at lower injection velocities (larger injection ports) failed to raise the mmr limit. No variation was imposed on the temperature of the hydrogen for two reasons. First the supply of fuel was not great enough to begin a new series of tests. Second, much of the attractiveness in the system due to simplicity is lost if the hydrogen must be preheated.

The most probable explanation for the limit in mmr attributes an unacceptable heat loss from the decomposing methyl acetylene to the incoming hydrogen. This ability of the hydrogen can be realized by comparing the heat available in the monopropellant reaction and comparing it to the heat required to raise the hydrogen to a temperature near the measured chamber temperature. Using this overly simplified approach it is seen that approximately half of the heat available is required to increase the hydrogen temperature. It would be necessary to investigate the reaction kinetics to determine the actual balance of heat production and absorption that ultimately determines whether the combustion would extinguish. The injection of hydrogen in a gradual ramp was then chosen as the experimental approach to probe this balance.

The inability of the ramp technique to determine a precise maximum value in mmr was attributed to experimental scatter (of the order of $4.0 \pm .2$ mmr).

Representative data for the operational limits can be found in the table below. These two listings are typical of several test runs at each mmr.

mmr	c*	T_c	Product Composition % CH_4	% H_2	% C(s)
0	2750 fps	2250°F	18	18	64
3.6	4700	2100	45	34	21

After obtaining these data, a calculation was made to check the normally assumed adiabatic nature of a rocket. It was found that neither of the above cases correspond to adiabatic operation, but in fact a 30% heat loss was associated with the monopropellant mode and an 18% loss with mmr = 3.6 operation. Such losses were suspected because the fuel flow rates were very low for economy reasons and the combustion chamber was constructed with thick copper walls. Since a more meaningful evaluation of a rocket system can be made from the adiabatic condition, a scheme was introduced to correct the data that were obtained. An iterative procedure was derived to change the chamber temperature, and thus alter the related reaction kinetics, until the adiabatic condition was achieved[21]. The results of the procedure indicated the existence of the following modified conditions:

mmr	c*	T_c	Product Composition % CH_4	% H_2	% C(s)
0	3200 fps	2900°F	10	27	63
3.6	5000	2100	35	40	25

CONCLUSIONS

From this experimental program several principal conclusions may be drawn.

(1) the addition of hydrogen to the decomposition reaction of methyl acetylene does provide increases both in rocket performance and methane content in the exhaust gases; and

(2) it appears that an upper operational limit on mmr exists which is well below the most desirable operating point; and

(3) the goals of low temperatures, high performance, and combustible exhaust products were shown to be achieved only in part.

Only for the exceptional application (e.g. where H_2 boiloff might be utilized) might one expect this concept to be employed based on the promise shown to date.

VIII. CONCLUDING REMARKS

The use of quarter-wave tubes as a means to damp combustion instability was shown to have several advantages and disadvantages, when compared to the Helmholtz resonator designs. A higher peak of the real part of the admittance, indicating improved damping, is limited to a very narrow frequency band. The ability of the quarter-wave tube to damp the odd higher frequency modes can, at times, be used to advantage. Effective use of volume in the quarter-wave tube configuration allows additional damping units to be employed and carries the range of application to lower frequencies. These characteristics are useful in that they increase the flexibility of applying various damping devices in a particular application. Experiments are confirming the theoretical findings.

Experimental and theoretical results from the different flame studies continue to indicate that the response of the wake of a burning droplet to velocity oscillations may be large enough to drive combustion instability. The experimental program to probe the fluctuating flame is quite complex since the accuracy is very demanding and often the measurement means is at the limits of the state-of-the-art. Similar experimental difficulties were overcome in the mass-energy sources research. There, through the use of experimental measurements of the pressure time-history of the step-shaped shock pulse tracer, a knowledge of the prior steady-state combustion conditions, the shock relations, and using the one-dimensional conservation equations, mass-energy source distributions have been determined. The sources vary with axial position in the rocket chamber as would be expected.

The analytical study of annular chambers so as to properly formulate the mechanisms responsible for combustion instability and predict the final wave shapes that would result has progressed considerably. The numerical results are indeed

revealing the anticipated shock-type waves. As parameters are varied certain stability trends have become evident.

Sampling of the combustion products of the hydrogenation rocket have revealed that the improved performance is a resultant of the hydrogen acting as a working fluid rather than the desired fundamental chemical changes. These data tend to discourage further work based on the hydrogenation approach.

NOMENCLATURE

a	Velocity amplitude (see pg. 16)
A	Orifice cross-sectional area
A,B,D	Constants in Sect. VI
b	Steady-state length of the combustion zone
c	Speed of sound
c_{1a}	Average chamber speed of sound
$c_{1\ell}$	Chamber speed of sound local to the lined surface
c_p	Specific heat of gases
C	Constant in Sect. VI
C_D	Discharge coefficient
Ch	Hyperbolic cosine
C_p	Pressure coefficient
d	Orifice diameter of Helmholtz resonator
D	Helmholtz cavity diameter (Sect. III) Burner diameter (Sect. V)
$\mathcal{E}_R$	Real part of the nozzle admittance
f	Frequency Frequency ratio (Sect. III)
f_L	Fraction of the chamber wall area lined
$g(\theta)$	RHS of Eq. 12, pg. 63
G	Defined in equation on pg. 25, related to the in phase energy addition in the combustion chamber
I_{sp}	Specific impulse
ℓ	Length of Helmholtz resonator orifice Combustion chamber length
L	Length of Helmholtz cavity
$\mathcal{L}$	Acoustic admittance
$\mathcal{L}_I$	Imaginary part
$\mathcal{L}_R$	Real part

$\dot{m}_b$	Instantaneous mass burning rate
M	Defined by equation on pg. 25
$\bar{M}_e$	Mean chamber Mach number at nozzle entrance
$M(\theta)$	Integral term of Eq. 8, pg. 63
MW	Molecular weight
n	Interaction index
p	Pressure
q	Magnitude of vector velocity
$\underline{q}$	Vector velocity
$\underline{q}_\ell$	Liquid vector velocity
$\underline{q}_{\ell i}$	Injection velocity
q_{rel}	Velocity of droplet relative to the gas
Q	Dimensionless unsteady mass-energy source
Sh	Hyperbolic sine
$S_{\nu\eta}$	Eigenvalue describing instability mode (Tables A-1,2 Ref. 10)
t	Time
T	Temperature in chamber
u	Local gas velocity Gas velocity in quarter-wave tube (Sect. III) Axial velocity component (Sect. V)
$u_{\ell i}$	Axial component of liquid velocity
u_n	Nozzle entrance axial velocity
v	Radial velocity component (Sect. V) Circumferential velocity component (Sect. VI)
$\vec{v}$	Gas streaming velocity
$\vec{v}_{flame}$	Velocity of flame surface
$\vec{v}_{rel}$	Fuel flow velocity relative to the flame front

V	Helmholtz cavity volume Volume ratio of the droplet (relative to its injection volume) (Sect. VI)
$\vec{V}_F$	Fuel diffusion velocity
W	Defined by equation on pg. 10
x	Axial space coordinate
X	Chamber length (or combustion length if less than chamber length)
y	Circumferential variable
Y_F	Mass fraction fuel at flame surface
α	Mean gas velocity in the chamber
β	Ratio of nozzle entrance velocity to the liquid velocity $\frac{\bar{u}_n}{\bar{u}_\ell}$
γ	Ratio of specific heats
γ_{ia}	Average value of the specific heats in the chamber
δ_u	Phase angle between gas velocity and pressure oscillations in the chamber
ϵ	Pressure oscillation amplitude
ϵ_o	Maximum value of the square root of the non-dimensional pressure amplitude
θ	Equivalent to ft-y
θ'	Dummy variable used on pg. 64
θ^*	Singular point
λ	Wavelength
μ	Injection rate per unit area
ν	Integer describing tangential character of mode (Table A-1,2, Ref. 10)
ξ	Dummy variable
ρ	Gas density
σ	Percent open area ratio of lined surface

τ	Sensitive time lag Droplet lifetime (Sect. VI)
ϕ	Arbitrary function
Φ	Function of θ (pg. 65)
ω	Angular frequency of instability, radians

Subscripts

I	Imaginary part
m	Arithmetic mean value at the shock (Sect.VI)
R	Real part
t	Derivative with respect to time $d(\ )/dt$
1,2,...	Order of series expansion (Sect.VI)
1	Pertaining to the chamber
2	Pertaining to the entrance
3	Pertaining to the quarter-wave tube end

Superscripts

$(\bar{})$	Mean or steady-state value
$(\ )'$	Perturbation
$(\vec{})$	Vector
$(\underline{})$	Vector (Sect. VI)
$(\ )^+$	Inward flow
$(\ )^-$	Outward flow
$(\hat{})$	Transformed dependent variables

REFERENCES

1. Sirignano, W. A., "The Nonlinearity of Acoustic Liners". To be published. See also "Nonlinear Aspects of Combustion Instability in Liquid Propellant Rocket Motors," Sixth Yearly Report), Princeton University Dept. of Aerospace and Mechanical Sciences Report No. 553-F, June 1966.

2. Tonon, T. S. and Sirignano, W. A., "Near-Resonant, Off-Resonant, and Quasi-Steady Theories of Acoustic Liner Operation," Sixth ICRPG Combustion Conference, CPIA Pub. No. 192, Vol. 1, Dec. 1969, pp. 249-256.

3. Tonon, T. S. and Sirignano, W. A., "The Nonlinearity of Acoustic Liners with Flow Effects," AIAA Paper No. 70-128, AIAA Eighth Aerospace Sciences Meeting, January, 1970.

4. Ingard, U., "On the Theory and Design of Acoustic Resonators," J. Acoustical Soc. Amer., Vol. 25, No. 6, Nov. 1953, pp. 1037-1067.

5. Ingard, U. and Ising, H., "Acoustic Nonlinearity of an Orifice," J. Acoustical Soc. Amer., Vol. 42, No. 1, June 1967, pp. 6-17.

6. Crocco, L., Harrje, D., Sirignano, W. A., et al, "1969 Summary of Combustion Instability Research at Princeton University," NASA CR 72680, 1970, pp. 16-22.

7. Tang, P. K. and Sirignano, W. A., "Theoretical Studies of Quarter-Wave Tube," AIAA Paper No. 71-87, AIAA Ninth Aerospace Meeting, January 1971.

8. Bogdanoff, D. W., "A Study of the Mechanisms of Heat Transfer in Oscillating Flow," Technical Report No. 483-f, Dept. of Aerospace and Mechanical Sciences, Princeton University, 1967.

9. Lloyd, R. M., "Optimum Placement of Helmholtz Resonators for Damping Pressure Oscillations," MSE Thesis, Dept. of Aerospace and Mechanical Sciences, Princeton University, 1968.

10. Tonon, T. S., Sirignano, W. A. and Harrje, D. T., "Fluid Mechanics Approach to Acoustic Liner Design," NASA CR 72807, December 1970.

11. Bracco, F. V. and Harrje, D. T., "The Direct Method Applied to Steady Liquid Propellant Combustion: Investigation of Several Droplet Burning Models for a LOX/Ethanol Engine," 6th ICRPG Combustion Conference, CPIA Pub. No. 192, Vol. 1, December 1969, pp. 85-91.

12. Bracco, F. V., "The Direct Method as Applied to Liquid Rocket Engine Combustion and Explosion Problems", Ph.D. Thesis, Princeton University, Princeton, N. J., June 1970.

13. Crocco, L., "Theoretical Studies on Liquid Propellant Rocket Instability," Tenth Symposium (International) on Combustion, The Combustion Institute, 1965, p. 1101.

14. Strahle, W. C., "Unsteady Laminar Jet Flame at Large Frequencies of Oscillation," AIAA J., Vol. 3, No. 5, May 1965, p. 957.

15. Feiler, C. E. and Yeager, E. B., "Effect of Large Amplitude Oscillation on Heat Transfer," NASA TR R-142, 1962.

16. Lemlich, R. and Hwu, C. K., "The Effect of Acoustic Vibration on Forced Convective Heat Transfer," A.I. Ch. E. Journal, Vol. 7, March 1961, pp. 102-106.

17. Crocco, L., "Research on Combustion Instability in Liquid Propellant Motors," Twelfth Symposium (International) on Combustion, published by the Combustion Institute, Pittsburgh, Pa., 1969, p. 85.

18. Glassman, I., "Method of Producing Thrust by Hydrogenation of an Acetylenic Hydrocarbon", U. S. Patent No. 3, 170,281.

19. Rosfjord, T., "Hydrogenation as an Energy Source", NASA CR 72680, February, 1969, pp. 75-79.

20. Glassman, I., "Hydrogenation - A New Concept for Propellant Selection (The Acetylene-Hydrogen Combination)", Air Reduction Company, Inc.

21. Nesbit, E., "Summary of Investigations into Hydrogenation as a Rocket Energy Source", Report of Junior Year Independent Research, Princeton University, October 12, 1970.

LIST OF FIGURES

1970 DISTRIBUTION LIST

Dr. R. J. Priem MS 500-204
NASA Lewis Research Center
21000 Brookpark Road
Cleveland, Ohio 44135 (2)

Norman T. Musial
NASA Lewis Research Center
21000 Brookpark Road
Cleveland, Ohio 44135

Library
NASA Lewis Research Center
21000 Brookpark Road
Cleveland, Ohio 44135 (2)

Report Control Office
NASA Lewis Research Center
21000 Brookpark Road
Cleveland, Ohio 44135

NASA Representative
NASA Scientific and Technical
Information Facility
P.O. Box 33
College Park, Maryland 20740 (6)

NASA
Universal North Building
Connecticut & Florida Avenues
Washington, D. C. (10)
Attn: Dr. T. L. Smull, Director
Grants & Space Contracts

V. Agosta
Brooklyn Polytechnic Institute
Long Island Graduate Center
Route 110
Farmingdale, New York 11735

B. P. Breen
Dynamic Science, a Division of
Marshall Industries
1900 Walker Avenue
Monrovia, California 91016

Thomas J. Chew
AFRPL(RPPZ)
Edwards, California 93523

T. W. Christian
Chemical Propulsion Information
Agency
8621 Georgia Avenue
Silver Spring, Maryland 20910

R. M. Clayton
Jet Propulsion Laboratory
California Institute of
Technology
4800 Oak Grove Drive
Pasadena, California 91103

E. W. Conrad MS 500-204
NASA Lewis Research Center
21000 Brookpark Road
Cleveland, Ohio 44135

Dr. E. K. Dabora
University of Connecticut
Aerospace Department
Storrs, Connecticut 06268

O. W. Dykema
Aerospace Corporation
P.O. Box 95085
Los Angeles, California 90045

G. W. Elverum
TRW Systems
1 Space Park
Redondo Beach, California 90278

R. Edse
Ohio State University
Dept. of Aeronautical and
Astronautical Engineering
Columbus, Ohio 43210

G. M. Faeth
The Pennsylvania State University
Mechanical Engineering Department
207 Mechanical Engineering Blvd.
University Park, Pa. 16802

G. D. Garrison
Pratt and Whitney Aircraft
Florida Research and Development
Center
P.O. Box 2691
West Palm Beach, Florida 33402

M. Gerstein
Dept. Mech. Engr.
University of Southern
California
University Park
Los Angeles, California 90007

I. Glassman
Princeton University
Forrestal Campus
Princeton, New Jersey 08540

R. W. Haffner
Air Force Office of Scientific
Research
1400 Wilson Blvd.
Arlington, Virginia 22209

D. Harrje
Princeton University
Forrestal Campus
Princeton, New Jersey 08540

T. Inouye Code 4581
U. S. Naval Weapons Center
China Lake, California 93555

R. D. Jackel, 429
Office of Naval Research
Navy Department
Washington, D. C. 20360

R. B. Lawhead
Rocketdyne
A Division of North American
Aviation
6633 Canoga Avenue
Canoga Park, California 91304

R. S. Levine, Code RPL
NASA Headquarters
6th and Independence Ave., S.W.
Washington, D. C. 20546

Ted Male MS 500-209
NASA Lewis Research Center
21000 Brookpark Road
Cleveland, Ohio 44135

J. M. McBride
Aerojet-General Corporation
P.O. Box 15847
Sacramento, California 95809

P. D. McCormack
Dartmouth University
Hanover, New Hampshire 03755

C. E. Mitchell
Colorado State University
Fort Collins, Colorado 80521

P. S. Myers
University of Wisconsin
Mechanical Engineering Dept.
1513 University Avenue
Madison, Wisconsin 53705

J. A. Nestlerode
Rocketdyne
A Division of North American
Aviation
6633 Canoga Avenue
Canoga Park, California 91304

J. A. Nicholls
University of Michigan
Aerospace Engineering
Ann Arbor, Michigan 48104

J. C. O'Hara
Tulane University
Dept. of Mechanical Engr.
New Orleans, La. 70118

A. K. Oppenhiem
University of California
Dept. of Aeronautical Sciences
6161 Etcheverry Hall
Berkeley, California 94720

J. R. Osborn
Purdue University
School of Mechanical Engr.
Lafayette, Indiana 47907

Dr. K. Ragland
University of Wisconsin
Mechanical Engineering Dept.
Madison, Wisconsin 53705

Dr. A. A. Ranger
Purdue University
School of Aeronautics,
Astronautics and Eng. Sciences
Lafayette, Indiana 47907

F. H. Reardon
Sacramento State College
School of Engineering
6000 J. Street
Sacramento, California 95819

B. A. Reese
Purdue University
School of Mechanical Engr.
Lafayette, Indiana 47907

R. J. Richmond R-P and VE-PA
NASA George C. Marshall Space Flight Center
Huntsville, Alabama 35812

J. H. Rupe
Jet Propulsion Laboratory
California Institute of Tech.
4800 Oak Grove Drive
Pasadena, California 91103

Dr. R. F. Sawyer
University of California
Mechanical Engineering, Thermal Systems
Berkeley, California 94720

K. Scheller
ARL(ARC)
Wright-Patterson AFB
Dayton, Ohio 45433

Roger A. Strehlow
University of Illinois
Aeronautical Engineering Dept.
Urbana, Illinois 61801

J. G. Thibadaux
NASA Manned Spacecraft Center
Houston, Texas 77058

T. P. Torda
Illinois Institute of Tech.
Room 200 M.H.
3300 S. Federal Street
Chicago, Illinois 60616

T. Y. Toong
Massachusetts Institute of Technology
Department of Mechanical Engr.
Cambridge, Massachusetts 02139

R. R. Weiss
AFRPL
Edwards, California 93523

W. W. Wharton AMSMI-RKL
U. S. Army Missile Command
Redstone Arsenal, Alabama 35808

F. A. Williams
University of California
Aerospace Engineering Dept.
P.O. Box 109
LaJolla, California 92038

L. M. Wood
Bell Aerospace Company
P.O. Box 1
Mail Zone J-81
Buffalo, New York 14205

B. T. Zinn
Georgia Institute of Technology
Aerospace School
Atlanta, Georgia 30332

Library
Goddard Space Flight Center (NASA)
Greenbelt, Maryland 20771

Library
NASA John F. Kennedy Space Center
Cocoa Beach, Florida 32931

Library
NASA Langley Research Center
Langley Station
Hamption, Virginia 23365

Library
NASA Manned Spacecraft Center
Houston, Texas 77001

Library
NASA George C. Marshal Space Flight Center
Huntsville, Alabama 35812

Library
Jet Propulsion Laboratory
4800 Oak Grove Drive
Pasadena, California 91103

Library
NASA Flight Research Center
P.O. Box 273
Edwards, California 93523

Library
NASA Ames Research Center
Moffett Field, California 94035

TISIA
Defense Documentation Center
Cameron Station
Building 5
5010 Duke Street
Alexandria, Virginia 22314

Office of Asst. Dir. (Chem. Tech.)
Office of the Director of Defense Research & Engineering
Washington, D. C. 20301

D. E. Mock
Advanced Research Projects Agency
Washington, D. C. 20525

Dr. H. K. Doetsch
Arnold Engineering Development Center
Air Force Systems Command
Tullahoma, Tennessee 37389

Library
Air Force Rocket Propulsion Laboratory (RPR)
Edwards, California 93523

Library
Air Force Rocket Propulsion Laboratory (RPM)
Edwards, California 93523

Library
Bureau of Naval Weapons
Department of the Navy
Washington, D. C.

Library
Director (Code 6180)
U. S. Naval Research Laboratory
Washington, D. C. 20390

APRP (Library)
Air Force Aero-Propulsion Laboratory
Research & Technology Division
Air Force Systems Command
United States Air Force
Wright-Patterson AFB, Ohio 45433

Technical Information Department
Aeronutronic Division of Philco Ford Corp.
Ford Road
Newport Beach, California 92663

Library-Documents
Aerospace Corporation
2400 E. El Segundo Blvd.
Los Angeles, California 90045

Library
Bell Aerospace, Inc.
Box 1
Buffalo, New York 14205

Report Library, Room 6A
Battelle Memorial Institute
505 King Avenue
Columbus, Ohio 43201

D. Suichu
General Electric Company
Flight Propulsion Lab. Department
Cincinnati, Ohio 45215

Library
Ling-Temco-Vought Corp.
P.O. Box 5907
Dallas, Texas 75222

Marquardt Corporation
16555 Saticoy Street
Box 2013 - South Annex
Van Nuys, California 91409

P. F. Winternitz
New York University
University Heights
New York, New York

I. Forsten
Picatinny Arsenal
Dover, New Jersey 07801

R. Stiff
Propulsion Division
Aerojet-General Corporation
P.O. Box 15847
Sacramento, California 95803

Library, Department 596-306
Rocketdyne Division of Rockwell
North American Rockwell Inc.
6633 Canoga Avenue
Canoga Park, California 91304

Library
Stanford Research Institute
333 Ravenswood Avenue
Menlo Park, California 94025

Library
Susquehanna Corporation
Atlantic Research Division
Shirley Highway & Edsall Road
Alexandria, Virginia 22314

STL Tech. Lib. Doc. Acquisitions
TRW System Group
1 Space Park
Redondo Beach, California

Prof. W. A. Sirignano
Princeton University
Forrestal Campus
Princeton, New Jersey 08540

Dr. David Altman
United Aircraft Corporation
United Technology Center
P.O. Box 358
Sunnyvale, California 94088

Library
United Aircraft Corporation
Pratt & Whitney Division
Florida Research & Development Center
P.O. Box 2691
West Palm Beach, Florida 33402

J. B. Large
Institute of Sound and Vibration Research
University of South Hampton
England

A. P. Chervinsky
Dept. of Aeronautical Engineering
Technion Israel Institute of Technology
Haifa, Israel

Dr. W. E. Strahle
Aerospace School
Georgia Institute of Technology
Atlanta 13, Georgia

Prof. F. E. Culick
California Institute of Technology
204 Karman Laboratory
Pasadena, California 91109

Dr. A. E. Fuhs
Chief Scientist
Aero-Propulsion Laboratory (AFSC)
Wright-Patterson Air Force Base
Dayton, Ohio 45433